nature communications

Article

https://doi.org/10.1038/s41467-026-69706-4

Tuning aromatic cage occupancy in prenyltransferases enables selective and efficient production of rare c-prenylated flavonoids

Received: 30 June 2025

Accepted: 6 February 2026

Ruiying Qiu[1,2,3,4,9], Huisi Huang[5,9], Junxi Chi[2,3,4], Longwei Gao[2,3,4], Qilin Gao[2,3,4], Min Li[6], Menghao Cai[7], Haishuang Yu[7], Shijie Wang[7], Zhilan Qian[7], Minchuan Jiang[5], Yu Liu[8], Bo Chen[1], Yang Zhou[5], Zhi-Min Zhang[5] & Jian-bo Wang[2,3,4]

C-prenylated flavonoids possess notable pharmaceutical potential, but their production is hindered by the challenging selective prenylation of their unstable polyphenolic cores. Natural prenyltransferases offer a direct route but suffer from low activity and incomplete mechanistic understanding. Here, we report a directed evolution strategy to reshape the active pocket of the prenyltransferase AtaPT, uncovering an aromatic cage that governs both regioselectivity and donor specificity. By tuning cage occupancy, we engineer three mutants with high chemo- and regioselectivity toward dimethylallyl diphosphate or geranyl pyrophosphate. Structural analysis and molecular simulations validate the role of the cage in guiding flavonoid prenylation. Notably, the aromatic cage mechanism observed in AtaPT is not unique and can be recapitulated in homologous enzymes. Introduction of the aromatic cage consistently enhances both activity and selectivity, confirming its crucial role. AtaPT mutants enable the efficient and scalable synthesis of 27 *C*-prenylated flavonoids, including 8 previously unreported compounds. With an integrated donor regeneration system, preparative-scale biotransformations achieve product titers up to 400 mg/L. This study establishes a selective and scalable biocatalytic platform for flavonoid prenylation and offers mechanistic insights for enzyme engineering.

Prenylated flavonoids represent a distinctive class of natural products, characterized by the attachment of lipophilic prenyl chains to various positions on flavonoid scaffolds (Fig. 1a). This structural diversification imparts a broad spectrum of biological activities, including anti-inflammatory[1], anti-bacterial[2], antioxidant[3], antitumor[4], antidiabetic[5] and enzyme inhibitory effects[6]. Owing to these properties, prenylated flavonoids have garnered growing interest as promising scaffolds for drug discovery, attracting attention from both academia and the pharmaceutical industry. Notably, the position, number, and structural diversity of prenyl side substituents play a critical role in modulating bioactivity[7]. Moreover, the structural diversity of prenyl side chains extends beyond variations in carbon chain length; it also encompasses both normal prenylation (attack at the C-1 primary center of the prenyl carbocation) and reverse prenylation (attack at the C-3 tertiary center of the prenyl carbocation), further expanding the structural repertoire of prenylated flavonoids (Fig. 1b). Therefore, the development of

A full list of affiliations appears at the end of the paper. e-mail: zhouyang@jnu.edu.cn; zhangzm@jnu.edu.cn; jwang2023@zju.edu.cn

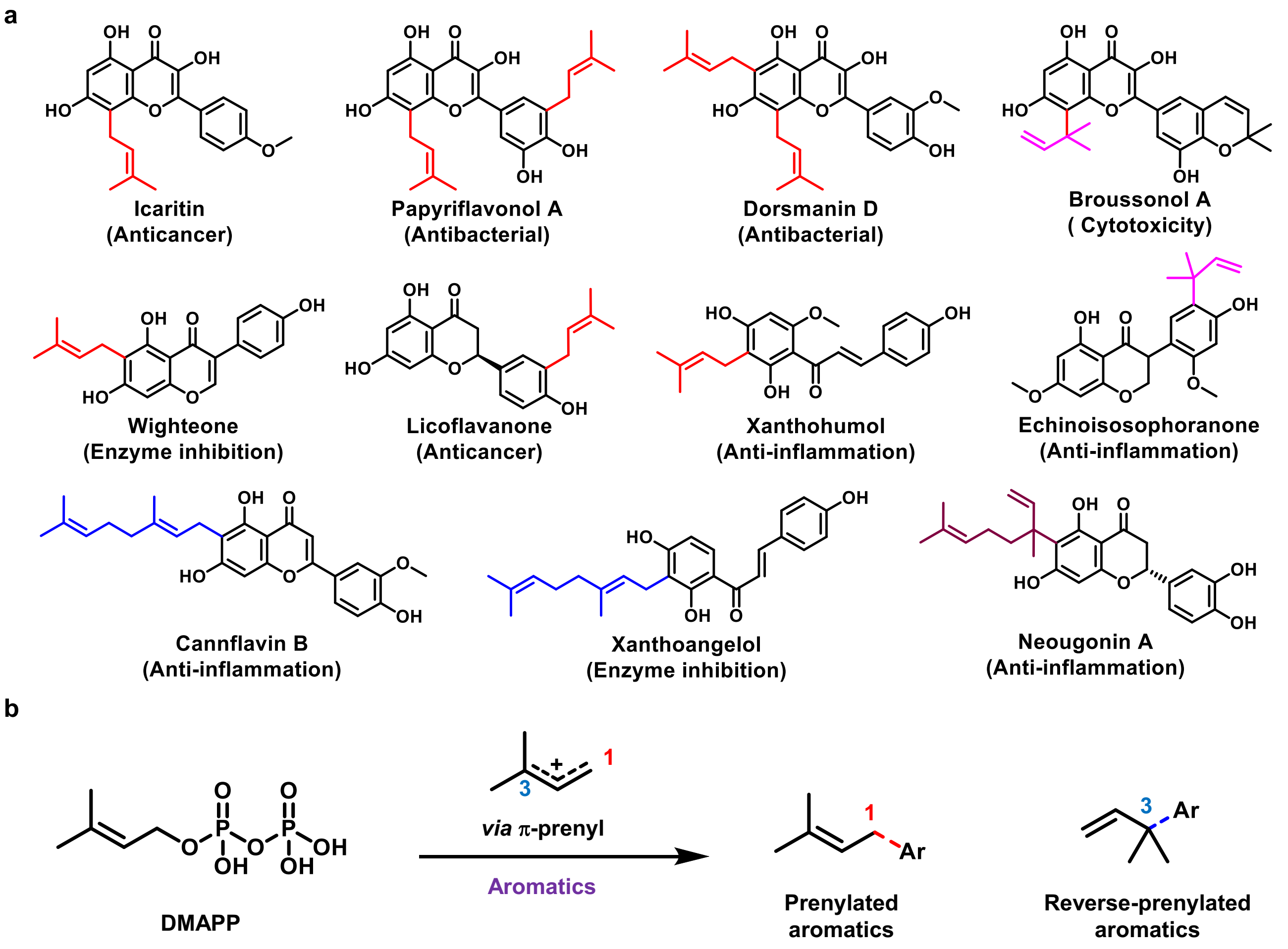

Fig. 1 | Common prenylated products. a Representative biologically active prenylated flavonoids. **b** Catalytic prenylation and reverse prenylation of aromatics. There are two types of the prenyltransfer reactions: 'normal' prenylation (attack at the *C*-1 primary centre of the prenyl carbocation) and 'reverse' prenylation (attack at the *C*-3 tertiary centre of the prenyl carbocation).

precise and efficient prenylation methodologies to obtain pure products is of paramount importance, particularly in pharmacal research and related fields.

To date, over 1000 naturally occurring prenylated flavonoids have been identified, however, their typically low abundance in nature often limits further investigation of their biological functions and therapeutic potential[8]. The inherent structural complexity of these secondary metabolites further complicates isolation and purification efforts. To address these challenges and obtain sufficient quantities of diverse, pure prenylated flavonoids, traditional organic synthesis methods—such as Friedel-Crafts alkylation[9], cross-coupling reactions[10], and rearrangement reactions[11], have been employed. Nevertheless, these approaches struggle to achieve precise selectivity and preserve the delicate flavonoid core under the harsh reaction conditions required. Recent advances in molecular biology, including gene sequencing and cost-effective synthesis, have significantly propelled the development of directed evolution technologies broadening the scope of biocatalysis[12–17]. Biocatalysis offers superior selectivity compared with traditional chemical synthesis, leading to a higher proportion of target products in the reaction mixture. This enhanced selectivity simplifies downstream purification and significantly reduces post-reaction processing costs, thereby improving the overall cost-effectiveness of the biocatalytic approach. Consequently, biocatalysis has emerged as a promising complement to chemical synthesis, offering high selectivity, mild reaction conditions, and environmental sustainability[18–20].

Among biocatalysts capable of alkylation, aromatic prenyltransferases (aPTs) have demonstrated utility in producing prenylated flavonoids using dimethylallyl pyrophosphate (DMAPP), geranyl pyrophosphate (GPP), or farnesyl pyrophosphate (FPP) as prenyl donor[21–24]. Prior studies have established aPTs as valuable tools for constructing flavonoid prenylation platforms, owing to their satisfactory selectivity across diverse flavonoid substrate[25–29]. However, their practical application is limited by low to moderate catalytic activity and poor tolerance for substrate concentrations exceeding 0.5 mM. Although numerous aPTs have been characterized in metabolic engineering[30–33] or evaluated for acceptor substrate scope[34–38], few investigations have elucidated the mechanisms governing their activity and selectivity. Fewer than 20 aPT crystal structures have been reported to date, with characterized substrate specificity largely confined to amino acids[39–41], dihydroxyl napthine[36,42–44] or olivetolic acid[19,45], and no studies have detailed structure-based substrate selectivity or regio- and chemoselectivity toward flavonoids. The sole mechanistic insight into regioselectivity engineering of an aPT was reported by Li and co-workers, who successfully switched the product regioselectivity of 5-dimethylallyl tryptophan synthase (5-DMATS) to 6-DMATS via structure-guided mutagenesis; however, this work focused on tryptophan, a structurally simpler substrate than flavonoids[46]. Thus, structure-and mechanism-guided engineering of aPTs for the selective prenylation of flavonoids remains largely underexplored[47]. The Dai group reported a prenyltransferase, AtaPT, from *Aspergillus terreus*, which exhibits remarkable substrate promiscuity toward a broad range of aromatic acceptors (up to 72 types) and prenyl donors (with prenyl residues up to 20 carbons). This enzyme provides a powerful biocatalytic tool for the synthesis of diverse prenylated compounds. Moreover, the structural elucidation of AtaPT has offered valuable insights for further engineering toward enzymes capable of constructing unique bioactive scaffolds[48]. Building upon this pioneering work, significant progress has been made in tailoring its selectivity toward flavonoids[49] and chalcones[50]. However, given its exceptional catalytic potential, a deeper understanding of the mechanisms governing its activity and selectivity is essential for establishing a versatile platform for efficient and selective prenylation.

In this work, we employed directed evolution to the AtaPT, yielding three mutants with exceptional regioselectivity, chemoselectivity and enhanced activity for the prenylation of kaempferol at the 8-site, 3′-site and for the 3′-site geranylation, respectively. Leveraging structural analysis and molecular dynamic simulations, we identified an aromatic cage structural motif that plays a critical role in modulating regioselectivity and catalytic activity of AtaPT mutants toward flavonoid substrates. By further expanding the substrate scope and enabling the large-scale synthesis of diverse prenylated flavonoid derivatives—facilitated by an in situ DMAPP and GPP regeneration system—we establish a versatile and scalable biocatalytic platform for regioselective flavonoid prenylation.

Results

Testing the Activity of the AtaPT-WT toward Kempferol

8-Prenylkaempferol (8p-KAE) is a direct precursor to the drug Icaridin (Fig. 2a). To date, only seven reported aromatic prenyl-transferases (aPTs) are capable of accepting kaempferol (KAE) as a substrate to produce 8p-KAE (Supplementary Table 6)[33,48,51–54], with the highest documented conversion reaching 65% at a low substrate concentration of 0.2 mM. To develop a more efficient biocatalytic route to 8p-KAE, broaden the spectrum of kaempferol prenylation products, and gain mechanistic insight into aPT-mediated regioselectivity, we selected kaempferol (**1a**) as a model substrate for directed evolution. AtaPT[48–50], an aPT known for its promiscuous chemo- and regioselectivity, was chosen as the starting enzyme for directed evolution.

To facilitate high-throughput screening, the use of whole cells as biocatalysts was deemed essential. Accordingly, wild-type AtaPT (AtaPT-WT) was expressed in *E. coli*, and the resulting cells were employed directly as catalysts. Using dimethylallyl diphosphate (DMAPP) as the prenyl donor, AtaPT-WT catalyzed the formation of four major products from **1a**, albeit with low total conversion (Fig. 2b). LC-MS analysis, supported by comparison with a commercial standard (Supplementary Fig. 1, 3 and 32), identified product **2a** as 8-prenylkaempferol, with a conversion below 1% and regioselectivity of only 34%. Additional products included *C*-prenylated derivatives **3a** and **4a** and an *O*-prenylated derivative (**5a**). To improve activity, regio-, and chemoselectivity, a semi-rational directed evolution strategy was subsequently implemented.

Directed evolution of AtaPT

To identify mutation hotspots, **1a** and DMAPP were sequentially docked into the crystal structure of wild-type AtaPT (PDB: 5KCG)[48]. Based on the resulting model (Supplementary Fig. 2), 22 residues within 5 Å of the active site G82, L83, E91, K95, R104, I167, E169, S170, C175, S177, D179, K188, L252, K266, L323, P324, G326, N328, Q342, R396, W397, and N411 were selected for site saturation mutagenesis (SSM)[55]. A total of 2,024 variants were expressed in *E. coli* and screened using whole-cell biotransformation in 96-deep-well plates, followed by product quantification via high-performance liquid chromatography (HPLC). Positive mutants were identified in 12 libraries (K95, I167, E169, S170, C175, S177, L323, P324, G326, N328, Q342, and W397). Among them, P324H exhibited the highest selectivity for **2a**, achieving 65.5% selectivity at a conversion of 0.5%. Examination of the P324 position in Supplementary Fig. 2 reveals that it is located near the B-ring of substrate **1a**. The substitution of the rigid proline residue with the positively charged aromatic residue histidine likely introduced an aromatic cage that facilitates accommodation of the B-ring of **1a**, contributing to the observed enhancement in regioselectivity when DMAPP severs as the donor. G326W showed markedly improved activity and selectivity for **3a**, reaching 16.6% conversion with 95.8% selectivity. Additionally, S177G preferentially produced **5a** with a conversion of 12.39% and selectivity of 46.2% (Supplementary Fig. 3 and Supplementary Table 8). Notably, both S177 and G326 had previously been implicated in modulating DMAPP binding and activity[48].

Building on the results from the initial cycle of directed evolution, further optimization was undertaken to enhance activity and selectivity. Iterative saturation mutagenesis (ISM)[56–59] was applied to nine promising residues——K95, I167, E169, S170, C175, L323, N328, Q342, and W397——using P324H, G326W, and S177G as templates. In parallel, four double-mutation libraries were constructed: P324H/G326NNK, P324H/S177NNK, G326W/P324NNK, and G326W/S177NNK. From this effort, the double mutant S177G/P324H was identified, exhibiting a conversion of 1.1% and a selectivity of 55.0% for **2a**. Iterative combinations led to the triple mutant S177G/P324H/N328M, which achieved a 5.5% conversion with 56.0% selectivity toward **2a**. In contrast, iterative mutagenesis based on G326W and S177G yielded less favorable outcomes, with no mutants surpassing the performance of their respective templates.

Given the limited improvement in yield from above efforts, we employed focused rational iterative site-specific mutagenesis (FRISM) [13,60–64], integrating insights from SSM and ISM to accelerate the discovery of superior variants. Subsequently, two combinatorial mutations sets were designed based on SSM and ISM results: K95/I167/E169/S170/C175 and E169/S170/S177/P324/N328 (Supplementary Table 7). This strategy generated the quintuple mutant E169A/S170Q/S177A/P324H/N328M (named as M5), which exhibited significantly enhanced activity (14.6% conversion) and selectivity (73.1%) toward **2a**. Using M5 as a template, further combinatorial mutagenesis at positions I167, C175, L323 and N328 produced the octuple mutant I167A/E169A/S170Q/C175M/-S177A/L323Q/P324H/N328R (named as M8), demonstrating the highest activity and regioselectivity for **2a** (44.5% conversion and 77.4% selectivity, Fig. 2d). In contrast, analogous efforts aimed at improving **3a** and **5a** formation did not yield superior variants.

Given the broad donor promiscuity of AtaPT, we next assessed its activity with GPP using **1a** as the acceptor. While the WT enzyme exhibited moderate selectivity for the 3′-geranylated product (**6a**) at 84.9%, overall conversion remained low (<14.6%). To enhance both catalytic efficiency and selectivity, selected variants from previous mutagenesis rounds were screened. The septuple mutant I167T/E169A/S170Q/S177A/L323Q/P324H/N328M (designated M7) demonstrated a dramatic improvement, achieving >90.7% conversion and 92.6% selectivity for **6a** (Fig. 2e). Notably, M7 was identified serendipitously during the second round of combinatorial mutagenesis, highlighting the effectiveness of the iterative strategy.

With the successful evolution of four functional mutants—G326W, M7, M8, and S177G—catalyzing the formation of three distinct *C*-prenylated KAE derivatives and one *O*-prenylated product, precise structural characterization was undertaken. This step was essential to confirm the exact prenylation sites and substitution patterns, thereby elucidating the chemo- and regioselectivity profiles of each engineered variant.

Structural Characterization of 2a, 3a, 4a, 5a, and 6a

To characterize the structures of **2a, 3a, 4a, 5a**, and **6a**, biotransformations were scaled up using whole-cell *E. coli* catalysts expressing the corresponding AtaPT mutants. Reactions were conducted at a 2 mM concentration of **1a** with 4 mM DMAPP (or GPP for **6a**) in 50 mL volumes. The isolated yields were 33.6% for **2a**, 12.2% for

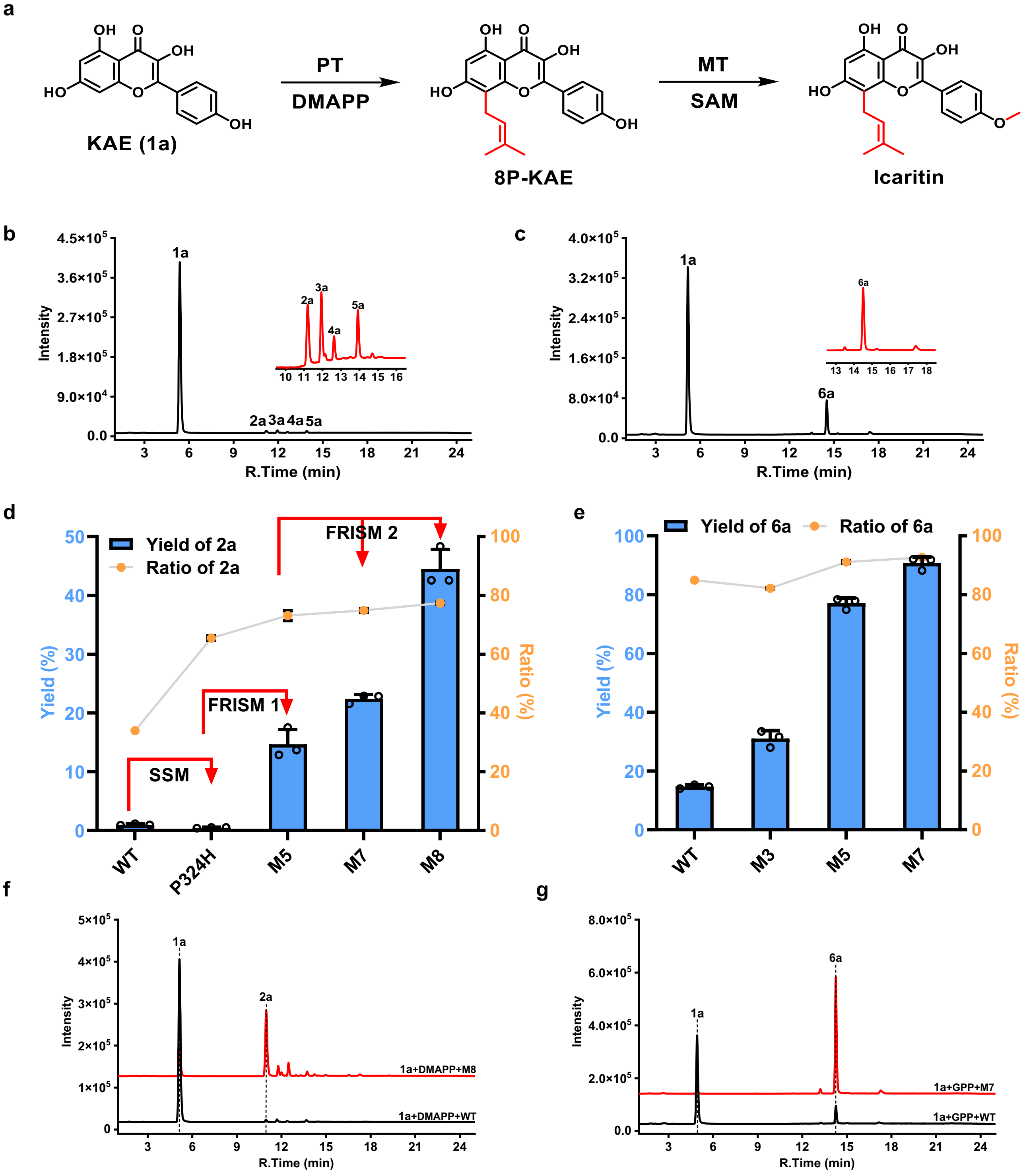

Fig. 2 | Evolution of AtaPT for efficient synthesis of prenylated kempferol derivatives. **a** Reactions starting with KAE to form 8P-KAE and Icaritin. **b** HPLC chromatogram showing the conversion of **1a** with DMAPP to products **2a, 3a, 4a**, and **5a** catalyzed by AtaPT-WT. **c** HPLC chromatogram of **1a** with GPP resulting in the formation of product **6a** catalyzed by AtaPT-WT. **d** Improvement in catalytic activity across five rounds of directed evolution using site-saturation mutagenesis (SSM), iterative saturation mutagenesis (ISM), and focused rational iterative site mutagenesis (FRISM). WT: wild type, M2: S177G/P324H, M3: S177G/P324H/N328M, M5: E169A/S170Q/S177A/P324H/N328M, M7: I167T/E169A/S170Q/S177G-/L323Q/P324H/N328M and M8: I167A/E169A/S170Q/C175M/S177A/L323Q/P324H/N328R. **e** Rescreening of mutants using GPP to enhance the conversion efficiency of (**6a**). **f** HPLC chromatogram showing the conversion of **1a** with DMAPP to products **2a**, catalyzed by AtaPT-M8. **g** HPLC chromatogram of **1a** with GPP resulting in the formation of product **6a** catalyzed by AtaPT-M7. Relative activities are reported as mean ± SD of three independent biological replicates ($n = 3$). The yield was determined by substituting the peak area into the standard calibration curve.

3a, 6.0% for **4a**, 9.1% for **5a**, and 78.4% for **6a**. The products were purified and structurally validated by NMR and high-resolution mass spectroscopy (HRMS). Spectroscopic analysis revealed that **3a** and **6a** are *C*-prenylated and *C*-geranylated, respectively, at the 3′-position of **1a, 4a** is *C*-prenylated at the 6-position of **1a**, while **5a** was identified as a 4′-*O*-prenylated derivative. Interestingly, **2a** was determined to be a rare reverse 8-prenylated kaempferol, differing from the anticipated 8p-KAE despite co-elution in HPLC (Supplementary Figs. 3, 55 and 56). This highlights the importance of rigorous structural elucidation in biocatalytic prenylation studies.

Kinetic Characterization of AtaPT Variants

To elucidate the catalytic basis underlying the enhanced performance of variants G326W, M8, and M7, steady-state kinetic assays were conducted using **1a** as the acceptor substrate. The wild-type AtaPT (WT) exhibited insufficient activity with dimethylallyl pyrophosphate (DMAPP) to reliably determine kinetic parameters. In contrast, M8 and G326W showed markedly improved catalytic efficiency, with k_{cat}/K_m value of 34.79 s^{-1} M^{-1} and 15.09 s^{-1} M^{-1}, respectively, using DMAPP as the donor. When geranyl pyrophosphate (GPP) was employed, M7 demonstrated both an increased turnover number ($k_{cat} = 0.64$ min^{-1}) and a reduced Michaelis constant ($K_m = 0.23$ mM) relative to WT ($k_{cat} = 0.09$ min^{-1}; $K_m = 1.27$ mM). As a result, the catalytic efficiency of M7 ($k_{cat}/K_m = 47.12$ s^{-1} M^{-1}) exceeded that of WT by over 40-fold (1.12 s^{-1} M^{-1}), indicating substantially improved substrate affinity and catalytic performance (Supplementary Table 9 and Supplementary Fig. 13). We investigated the stability of the purified enzymes M8, G326W, and M7 over extended reaction times. The reaction profiles showed that product formation plateaued after approximately 8 h. When additional DMAPP/GPP was supplemented at this point, a further increase in product yield was observed, indicating that enzyme activity was maintained beyond the initial reaction phase. To further confirm enzyme stability, the reaction supernatant was collected after 8 h, supplemented with a fresh substrate and DMAPP or GPP, and incubated further. The continued formation of the corresponding products demonstrated that the enzymes retained substantial catalytic activity over prolonged periods (Supplementary Fig. 14). These results suggest that the current limitation lies in donor substrate depletion rather than enzyme instability, highlighting the need for a more efficient donor regeneration system in future applications.

Crystal structure resolution, molecular docking and molecular dynamics simulations

To elucidate the molecular basis for the enhanced activity and regio-/chemoselectivity of engineered AtaPT variants, we determined the crystal structures of M8 (2.50 Å, PDB: 9V5G), G326W (2.69 Å, PDB: 9V5F) and M7 (2.20 Å, PDB: 9V3U) (Supplementary Table 10). Crystals of M8 were obtained in the apo form and subsequently soaked with DMSPP and **1a** for varying durations prior to data collection. The overall protein architecture remained largely unchanged relative to the wild-type AtaPT structure, except for a notable movement of DMSPP in M8 away from the substrate binding pocket (Fig. 3a). This rearrangement is attributable to the N328R mutation, whose guanidinium group forms dual hydrogen bonds with the two phosphate moieties, thereby stabilizing the altered geometry. The substrate-binding pocket remained solvent-accessible, with **1a** positioned at the base of the cavity. On one side of **1a**, the chromenone core was packed against P324H, Y344, W397 and Y413, forming an aromatic cage. Of these residues, the P324H mutation played a pivotal role in anchoring **1a** via a hydrogen bond, thereby reducing its conformational flexibility (Fig. 3b). This is consistent with the substantial increase in regioselectivity observed for **2a** in this variant (Fig. 2d). To further assess whether this mutation is irreplaceable, we substituted this position with other aromatic residues (F, W, and Y) as well as bulky residues (M and L) in the WT, M7, and M8. Enzymatic assays showed that both activity and selectivity were markedly reduced compared with the original variants (Supplementary Fig. 16), demonstrating that histidine at this position is uniquely optimal for the observed enhancement in catalytic performance. On the other side, the chromenone core and the phenolic group of **1a** were stabilized by C175M and L252, respectively. Furthermore, the side chains of E91 and R396 form additional hydrogen bonds with the chromenone core (Supplementary Fig. 17). These interactions together bring the C8 position of **1a** into close proximity with the C3 atom of DMSPP (5.2 Å). The hydrogen bond between E91 and the hydroxyl group on C7 may facilitate the attack of C8 on C3 of DMAPP, thereby promoting the formation of the unusual reverse product **2a** via M8.

In contrast to M8, no substrate was observed in the structure of M7, even though the crystals were soaked with **1a** and GSPP before harvest. The electron density for GSPP was continuous and intact in one protomer of the dimeric structure (Supplementary Fig. 17). While in the other protomer, we could only define the pyrophosphate part unambiguously, implying flexibility of the geranyl chain. To probe the molecular basis of M7's improved catalytic performance with geranyl pyrophosphate (GPP), we docked both **1a** and GPP into M7 and performed molecular dynamics (MD) simulations (Supplementary Fig. 18). The simulations demonstrated that **1a** can be stably accommodated within the active site, as supported by the narrow RMSD fluctuations of **1a** and GPP during the whole simulations (Supplementary Fig. 18a). The distance between the 3′-positions of **1a** and the electrophilic center of the geranyl donor keep steadily around ~5 Å (Supplementary Fig. 18b and 18c). The main anchoring residues for **1a** binding through hydrogen bond include E91, N172, S192 and H324 (Supplementary Fig. 18d and 18e). Notably, the extended geranyl chain of GPP projects into the aromatic cage (Fig. 3c). This spatial shift induces a distinct binding orientation, in which the phenolic group of **1a** becomes deeply buried at the base of the pocket, forming a stabilizing hydrogen bond with the carboxylate of. This interaction likely activates the phenol ring for nucleophilic attack at the *ortho* position, thereby favoring *C*3′-geranylation to yield **6a**. The chromenone ring adopts a partially solvent-exposed configuration, directed toward a surface-accessible channel formed by a flexible loop comprising residues 167–170 (Fig. 3d). Within this loop, the S170Q mutation introduces a glutamine side chain that intrudes into the channel, narrowing its aperture and potentially stabilizing the substrate by limiting its mobility. Additionally, the I167T and E169A mutations probably enhance loop flexibility, promoting favorable conformational adjustments for substrate engagement and retention. Collectively, these observations suggest that the 167–170 loop functions as a dynamic gating element that modulates substrate access and positioning, thereby contributing to M7's improved regioselectivity and activity in GPP-dependent *C*3′-geranylation of **1a**.

Structural and computational analyses collectively reveal two distinct binding conformations of **1a** within the AtaPT substrate-binding pocket, which correspond to prenylation at either the chromone ring (conformation I) or the phenolic moiety (conformation II). Conformation I is stabilized by the combined effects of the C175M mutation and the aromatic cage introduced by P324H mutation. The aromatic cage appears essential for establishing this conformation, as its occupation or disruption triggers a switch to conformation II, favoring prenylation on the phenolic moiety. This mechanistic insight explains the regioselectivity observed for the M7 and G326W mutants. Specifically, in M7, the aromatic cage is occupied by the extended geranyl chain of GPP, whereas in G326W, the cage is disrupted due to the absence of the P324H mutation (Supplementary Fig. 19a). Furthermore, the bulky indole ring introduced by the G326W mutation occupies the cage's center, accounting for this mutant's exclusive preference for DMAPP as the prenyl donor, consistent with experimental observations showing no activity with GPP.

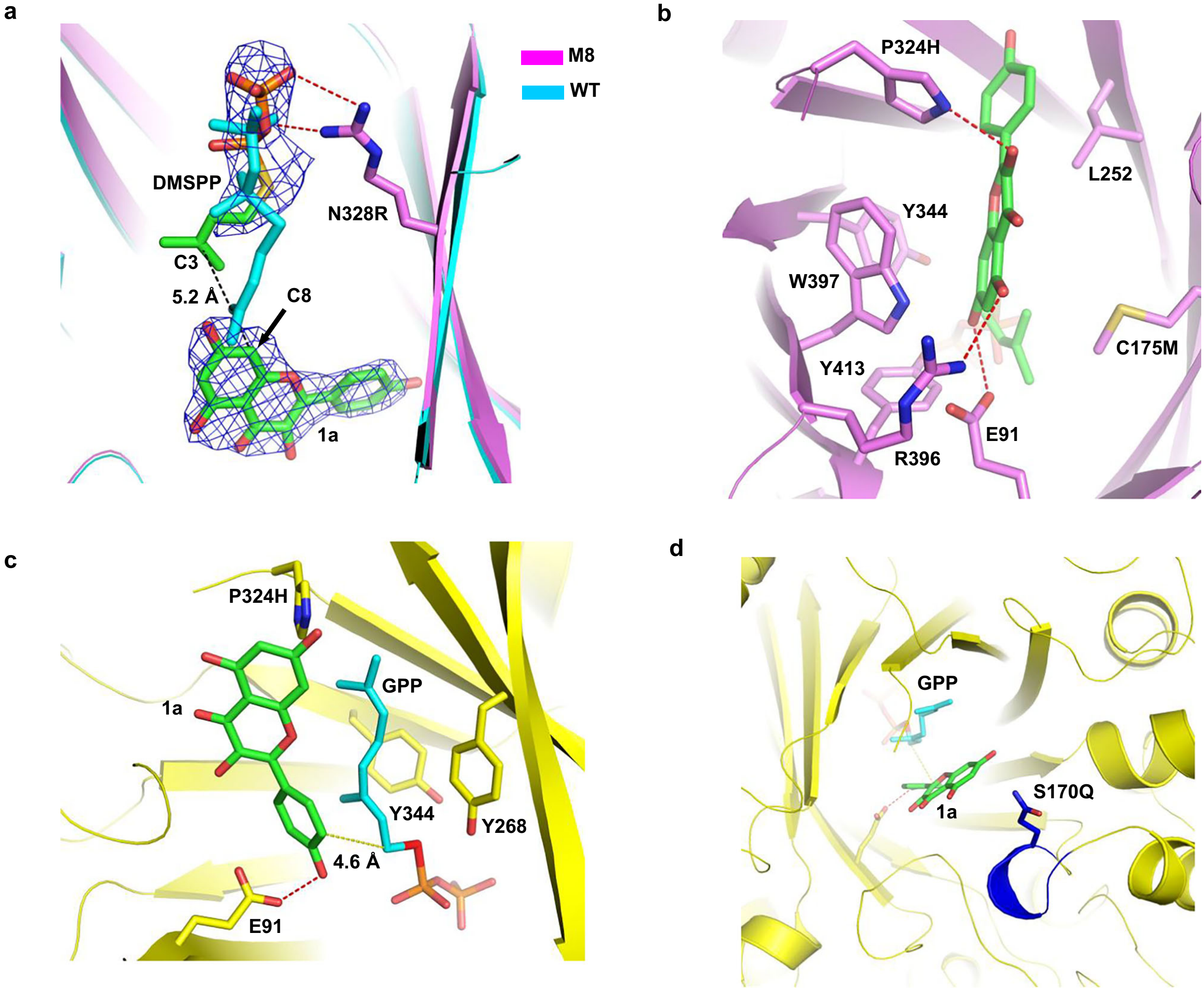

Fig. 3 | **Structural analysis of M8 and M7. a** 2fo-fc electron density map of **1a** and pyrophosphate in the crystal structure of M8 are shown at a contour level of 1.0 σ. Hydrogen bonds are shown as red dash. DMSPP in the WT AtaPT-DMSPP structure (PDB code: 5KCL) is shown as cyan stick. C8 position on **1a** was labeled. **b** The binding pocket of **1a**. The distance between C175M and **1a** is shown as yellow dash. **c** The docking model of **1a** and GPP in the active site of M7. **d** The loop containing residues 167-170 at the entrance of **1a** binding pocket.

The role of C175M is also indispensable for M8, as it may reduce the dynamics of **1a** and orientate the chromone ring for prenylation. This may be the reason why M7 cannot catalyze the prenylation of **1a** effectively as M8 (Fig. 2d and Supplementary Fig. 5), for the absence of C175M in M7 may result in a high degree of flexibility of **1a** in the pocket. When overlapping the M7-**1a** model with the structure of M8, the closest distance between the phenolic ring of **1a** and the C175M side chain is only 3 Å (Supplementary Fig. 19b), suggesting a potential steric clash. This observation explains why M8 exhibits very weak activity in modifying the 3′- position of **1a** using GPP as the donor, even lower than the WT.

Mechanism-guided design of PTs beyond AtaPT

The mechanisms of both the aromatic cage and the flexible loop have been elucidated; more importantly, it remains essential to determine whether the aromatic cage can be transferred to other PTs to guide the rational mining and design of enzymes with enhanced catalytic efficiency. Using AtaPT as a template for BLAST searches, we selected three homologous enzymes (Supplementary Table 11)—AfaPT (94.81% identity), AaaPT (86.70%), and AmaPT (56.87%)—all of which contain the conserved XXLPXX motif and a highly similar loop region (residues 167–170). We initially tested the WT activities of these enzymes toward kaempferol. With DMAPP, AfaPT-WT exhibited weak activity (1.7%) and produced **2a** as the major product (42.0%), whereas AaaPT-WT also showed low activity (1.3%) but favored **3a** (37.7%), with only 20.6% **2a.** AmaPT-WT showed similarly limited activity (1.4%) and generated only **3a** (56.1%) with no detectable **2a**. With GPP, AfaPT-WT and AaaPT-WT afforded **6a** with low activity (7.5% and 8.9%) but moderate selectivity (82.4% and 80.5%), whereas AmaPT-WT remained largely inactive (<1%) and produced only 7.5% **6a** (Fig. 4a).

According to our previous work on rationally tuning the chemoselectivity of glycosyltransferases, the substrate-binding mode governs both chemo- and regioselectivity[18]. To enhance catalytic performance and target-product formation, we first performed sequence and structural homologous comparisons using AtaPT-M8 and AtaPT-M7 as templates. For AfaPT and AaaPT, the active pockets were highly similar to that of AtaPT (Fig. 4b), suggesting that comparable catalytic properties could be achieved by introducing into these enzymes the key sites identified in AtaPT-M7 and AtaPT-M8 via site-directed mutagenesis. Guided by this strategy, we constructed AfaPT-M7, AfaPT-M8, AaaPT-M7, and AaaPT-M8. As anticipated, when tested with DMAPP, the M8 variants displayed dramatic increases in activity: AfaPT-M8 and AaaPT-M8 showed 14-fold and 19-fold increases in overall activity (22.9% and 25.6%) and 24-fold and 66-fold improvements in **2a**

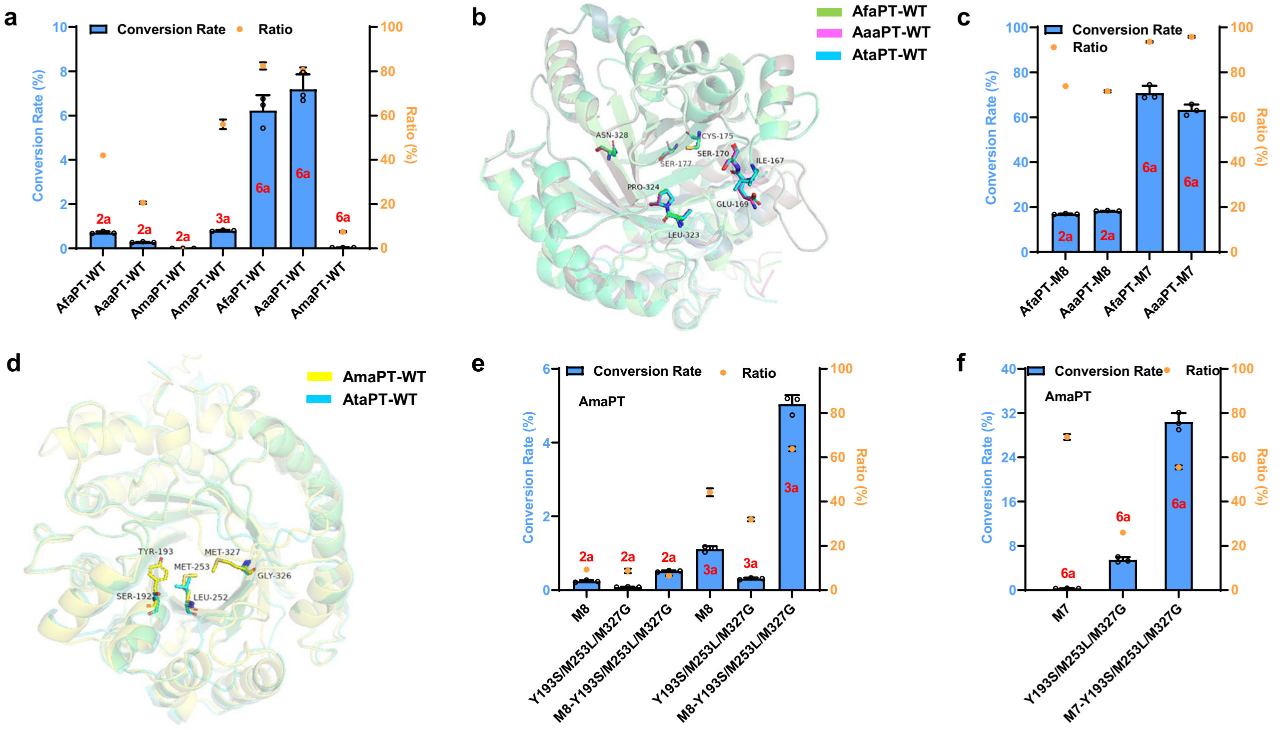

Fig. 4 | Mechanism-guided design of PTs beyond AtaPT. **a** Activity assays of AfaPT-WT, AaaPT-WT, and AmaPT-WT toward **1a** using DMAPP or GPP as the prenyl donor. **b** Structure alignment of AtaPT-WT with AfaPT-WT and AaaPT-WT. **c** Activity assays of AfaPT-M7 and AaaPT-M7 toward **1a** with GPP, and AfaPT-M8 and AaaPT-M8 toward **1a** with DMAPP. **d** Structure alignments of AtaPT-WT with AmaPT-WT. **e** Activity assays of AmaPT-M8, AmaPT-SLG and AmaPT-M8-SLG toward **1a** with DMAPP. **f** Activity assays of AmaPT-M7, AmaPT-SLG and AmaPT-M7-SLG toward **1a** with GPP. The crystal structure of AfaPT-WT, AaaPT-WT and AmaPT-WT was predicted by AlphaFold3. WT: wild type, AfaPT-M7: I167T/E169A/S170Q/S177G/L323Q/P324H/N328M, AaaPT-M7: I168T/Q170A/S171Q/S178G/L324Q/P325H/N329M, AfaPT-M8: I167A/E169A/S170Q/C175M/S177A/L323Q/P324H/N328R, AaaPT-M8: I168A/Q170A/S171Q/C176M/S178-A/L324Q/P325H/N329R, AmaPT-SLG: Y193S/M253L/M327G, AmaPT-SLG-M7: I168T/E170A/S171Q/S178A/Y193S/-M253L/L324Q/P325H/M327G/N329M and AmaPT-SLG-M8: I168A/E170A/S171Q/S176M/S178A/Y193S/M253L/L324-Q/P325H/M327G/N329R. Relative activities are reported as mean ± SD of three independent biological replicates ($n = 3$). The yield was determined by substituting the peak area into the standard calibration curve.

formation (16.9% and 18.3%), accompanied by substantially enhanced selectivity (73.8% and 71.6%; Fig. 4c). When tested with GPP, the M7 variants similarly improved catalysis: AfaPT-M7 and AaaPT-M7 increased overall activity to 75.6% and 66.0% and enhanced **6a** formation by 11-fold and 9-fold (70.7% and 63.2%), maintaining excellent selectivity (93.6% and 95.8%; Fig. 4c).

In contrast, the active pocket of AmaPT exhibited low homology to AtaPT and contained three bulky residues (Y193, M253, M327) that likely hindered productive binding of **1a** in a conformation favorable for generating **2a** (Fig. 4d). Therefore, improving the catalytic activity and selectivity of AmaPT required not only introduction of M7/M8 mutations but also remodeling of the pocket through substitution of these obstructive residues with the corresponding smaller residues found in AtaPT. To test this hypothesis, we constructed five variants: AmaPT-SLG (Y193S/M253L/M327G), AmaPT-M7, AmaPT-M8, AmaPT-M7-SLG, and AmaPT-M8-SLG. With DMAPP, AmaPT-M8 showed only modest overall activity improvement (2.5%) but enabled formation of **2a** for the first time (9.2%). As expected, AmaPT-SLG exhibited slightly reduced overall activity relative to AmaPT-WT yet produced **2a** with 8.7% selectivity. Notably, AmaPT-M8-SLG increased total activity to 7.9% and generated **2a** at levels sixfold higher than AmaPT-SLG and twofold higher than AmaPT-M8 (Fig. 4e).

When tested with GPP, AmaPT-M7 exhibited limited improvement in total conversion but increased **6a** formation ninefold with markedly enhanced selectivity (69.2%). Consistent with our design, AmaPT-SLG and AmaPT-M7-SLG produced greatly enhanced conversions (21.0% and 54.8%) despite moderate selectivity toward **6a** (26.0% and 55.4%; Fig. 4f). Ultimately, the optimized mutant AmaPT-M7-SLG increased **6a** formation by approximately 862-fold and improved selectivity nearly eightfold relative to AmaPT-WT, demonstrating that the aromatic cage mechanism discovered in AtaPT is transferable and can be effectively reconstituted in homologous PTs.

Substrate Scope Exploration

To evaluate the utility of AtaPT and its engineered *C*-prenyltransferase mutants for flavonoid prenylation, in vitro assays were conducted with 26 structurally diverse, medicinally relevant flavonoids (Supplementary Table 12). Consistent with prior reports[48], wild-type AtaPT (WT) catalyzed the prenylation of 23 out of 26 tested substrates, underscoring its broad substrate scope. However, under high substrate loading (2 mM), whole-cell catalysis by WT generally yielded low conversion and poor selectivity, with the exception of **1 g** and **1j**, which were efficiently converted to single prenylated products (>50% yield). Most other substrates yielded complex product mixtures in low abundance. Notably, neither WT nor the tested mutants (G326W, M5, M7, and M8) exhibited activity toward substrates **1t, 1 u**, and **1 v**. Comprehensive analysis of the reactions involving substrates **1t**–**1z** reveals that both the position and number of hydroxyl groups exert a pronounced influence on catalytic activity. Substrates **1t** (lacking hydroxyl groups), **1 u** (bearing one hydroxyl group on ring C), and **1 v** (bearing one hydroxyl group on ring A, possibly affected by an *ortho* effect) exhibited no detectable activity. Substrates **1w** and **1x**, each containing a single hydroxyl group on ring A, showed only weak activity. In contrast, substrates **1 y** and **1z**, each possessing a hydroxyl group on ring B, displayed relatively higher activity with mutants G326W and M7. These results indicate that the hydroxylation pattern

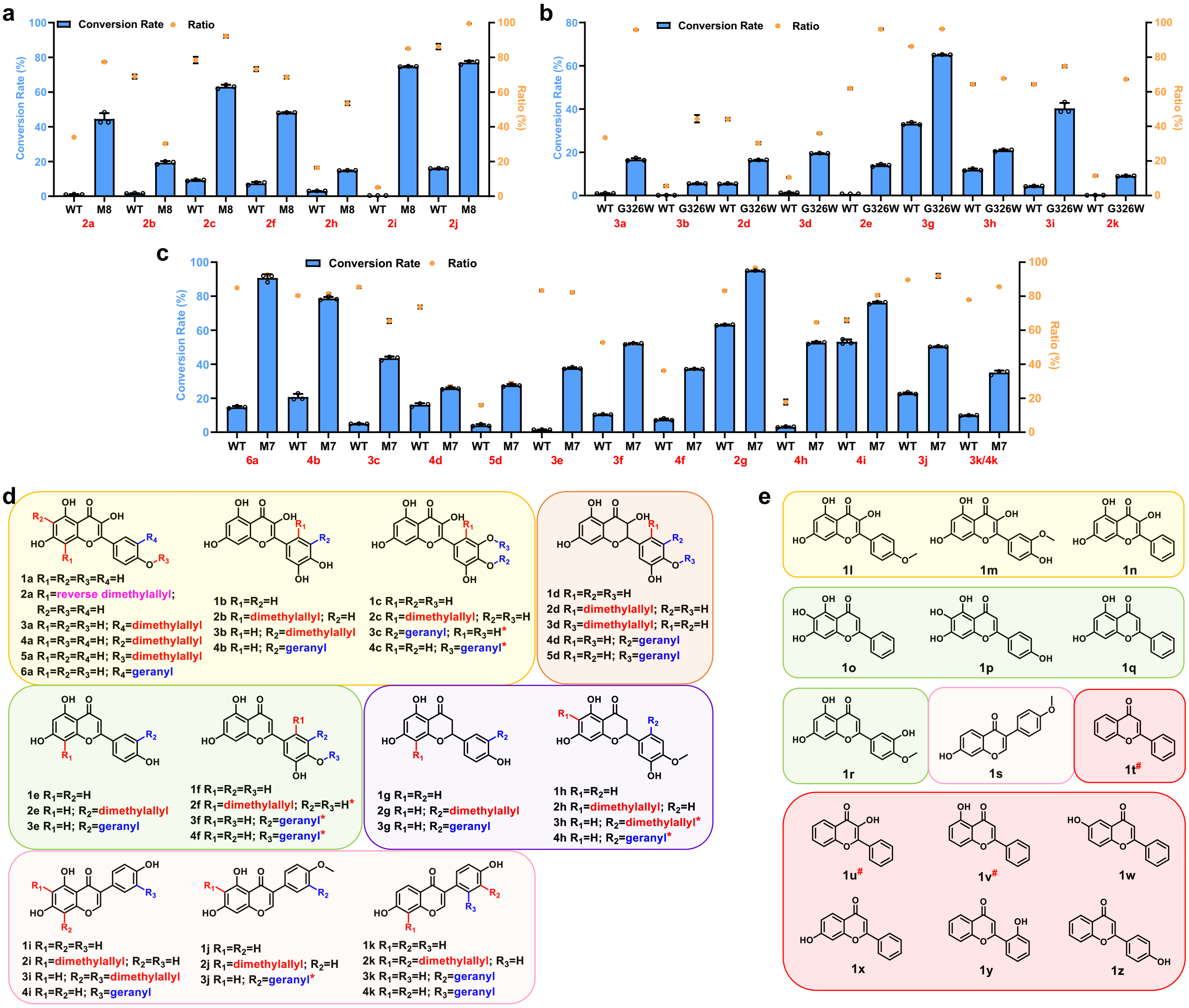

Fig. 5 | Exploration of substrate scope with AtaPT mutants. a Conversion and selectivity of selected flavonoids using DMAPP as the prenyl donor catalyzed by M8. **b** Conversion and selectivity of selected flavonoids using DMAPP as the prenyl donor catalyzed by G326W. **c** Conversion and selectivity of selected flavonoids using GPP as the prenyl donor catalyzed by M7. Bar graphs represent the conversion to the primary prenylated product, while dots indicate its relative proportion among total products; data were obtained by HPLC analysis excluding trace products (yield <1%). Experiments were performed in triplicate with standard deviations (s.d.) indicated. **d** Summary of all prenylation product types obtained from high-reactivity substrates. Biotransformations were conducted with 2 mM prenyl acceptor, 4 mM prenyl donor (DMAPP or GPP), 5 mM $CaCl_2$, and whole cells at an OD_{600} of 80, in 300 μL reaction volumes containing 6–8% (v/v) DMSO and 50 mM Tris-HCl buffer (pH 7.5). Reactions proceeded for 8–10 h, and products were isolated and characterized by HRMS as well as ^1H and ^{13}C NMR spectroscopy. **e** Structures of low-reactivity substrates tested under conditions with 0.5 mM acceptor, 1 mM prenyl donor (DMAPP or GPP), 5 mM $CaCl_2$, and whole cells (OD_{600} = 80) in a 300 μL reaction volume with 6–8% (v/v) DMSO and 50 mM Tris-HCl buffer (pH 7.5). Reactions proceeded for 8–10 h, and products were detected by HRMS. WT: wild type, M7: I167T/E169A/S170Q/S177G/L323Q/P324H/N328M and M8: I167A/E169A/S170Q/C175M/S177A-/L323Q/P324H/N328R. Relative activities are reported as mean ± SD of three independent biological replicates (n = 3). The conversion rate was calculated as the ratio of the product peak area to the substrate peak area determined by the HPLC. * These products have not been reported previously. # These substrates show no appreciable reactivity.

critically correlates with enzymatic performance, and substrates with hydroxyl substitution on the B ring generally exhibit broader enzyme compatibility and enhanced activity (Supplementary Fig. 23).

In contrast, M8 displayed markedly improved activity and regioselectivity across seven substrates (**1a**–**1c**, **1 f**, **1h**–**1i**), as confirmed by product isolation and NMR spectroscopic analysis. For **1a**, M8 catalyzed formation of the rare reverse 8-prenylkaempferol (**2a**). Substrates **1b, 1c** and **1 f** yielded 2′-prenylated products (**2b, 2c** and **2 f**), attributed to the influence of multiple hydroxyl groups on the B ring guiding substrate orientation. For **1 h**, bearing a methylated 4′-hydroxyl, prenylation occurred at the 6-position rather than the canonical 8-position. Isoflavones **1i** and **1j**, characterized by an inverted B-ring topology, were converted to 6-prenylated derivatives. M8 also exhibited moderate reactivity toward additional substrates, including **1 g**, for which it generated a broader range of products, likely reflecting enhanced conformational adaptability in the active site. In contrast, low activity toward **1e, 1k**, and **1 s** was attributed to the limited number of hydroxyl groups, weakening enzyme–substrate interactions (Fig. 5a and Supplementary Fig. 24).

The G326W mutant also prenylated eight substrates (**1a**–**1b, 1 d, 1e, 1g**–**1i, 1k**) with enhanced activity and regioselectivity compared to WT. Products from **1a, 1b, 1e**, and **1 g** were predominantly 3′-prenylated. The two products of **1 d** are respectively located at the 2′ and 4′-*O*-positions. Notably, **1 h** yielded a 2′-substituted product, attributed to the methylation of the 4′-hydroxyl. Isoflavones **1i** and **1k** were converted into diprenylated derivatives with modifications at both the 3′-

and 8-positions, suggesting that G326W reorients the B ring to facilitate proximity to DMAPP. Substrates **1c** and **1 f** showed limited reactivity, likely due to steric hindrance from B-ring hydroxylation, while **1l**–**1o** and **1q**–**1r** exhibited minimal conversion, presumably due to the absence or masking of key hydroxyl groups required for catalysis (Fig. 5b).

M5 and M7 exhibited significantly enhanced activity with GPP as the prenyl donor. In particular, M7 catalyzed geranylation of 11 substrates with high efficiency and selectivity, generating more than 15 distinct products. For example, **1c**, bearing three hydroxyls on the B ring, yielded two *O*-geranylated products—**3c** (4′-*O*) and 4c (3′-*O*)—in a 3:1 ratio, although they could not be separated by conventional chromatography. Substrates **1 h** and **1j** gave rise to **4 h** (2′-substituted) and **3j** (6-substituted), respectively, consistent with altered binding geometries in the active site. Product from **1k** was not fully characterized due to co-elution, as it exists as a 1:1 mixture, the products are likely geranylation at either the 2′- or 3′-position. The remaining substrates yielded products predominantly prenylated at the 3′- position likely reflects the larger volume and flexible conformation of the active site, which accommodates GPP's extended isoprenoid chain (Fig. 5c).

Altogether, we successfully prepared and characterized 31 prenylated flavonoids. Notably, eight of these compounds (**2 f, 3c, 3 f, 3 h, 3j, 4c, 4 f**, and **4 h**) are previously unreported, thereby expanding the chemical diversity of this compound class and providing more molecular scaffolds for future studies.

Coupling the isopentenol utilization pathway with prenyltransferase for prenylflavonoid biosynthesis

Recent strategies to boost intracellular dimethylallyl diphosphate (DMAPP) levels have focused on optimizing the native mevalonate (MVA) and methylerythritol phosphate (MEP) pathways[65], as well as engineering synthetic isopentenol utilization pathways (IUPs)[66]. By fine-tuning precursor availability in concert with prenyltransferase (PT) activity, these approaches facilitate efficient and cost-effective prenylation, holding significant promise for industrial biocatalysis[67,68]. The IUP offers a streamlined alternative by bypassing complex central carbon metabolism, instead leveraging exogenously supplied isoprenol or prenol, which are converted to isoprenoid diphosphates via sequential phosphorylation. This decoupled system not only simplifies metabolic control but also reduces the metabolic burden on host cells, presenting a competitive advantage over traditional biosynthetic routes. Integration of the IUP with PTs such as ShFPT[69], NgFPT[70], AnaPT[71] and Ad03[72] have recently enabled the biosynthesis of diverse prenylated flavonoids. Building on this framework, we envision that coupling a multi-enzyme cascade for enhanced in vivo DMAPP production with engineered PT variants—such as the highly active and selective. M8 and G326W—can further increase production titers and reduce costs. Additionally, the biosynthesis of geranyl pyrophosphate (GPP) in vivo, when coupled with the M7 variant, provides a promising route to access geranylated flavonoid scaffolds. Together, these strategies establish a versatile and scalable platform for the sustainable biosynthesis of prenylated natural products with pharmaceutical and nutraceutical relevance.

To evaluate the practical applicability of the biocatalytic cascade system for preparative-scale prenylation, we initiated reactions using whole cells co-expressing the prenyltransferase variant M8 (pET28a-M8) and the donor biosynthesis module PCDF-AtIPK-EcPK[73]. However, even in small-scale reactions (300 µL), the conversion rate is also limited, at only 5.6%. Cell lysis significantly improved reaction performance, with the lysate exhibiting double (11.3%) the activity of whole cells, though still inferior to that observed with externally supplied DMAPP. To improve donor supply, alternative kinase systems were tested. MjIPK[74] and MTHIPK[75] were expressed in place of AtIPK, generating the constructs PCDF-MjIPK-EcPK (23.1%) and PCDF-MTHIPK-EcPK (15.3%). Among these, MjIPK showed superior activity, doubling the conversion rate compared to the AtIPK-based system. Consequently, PCDF-MjIPK-EcPK and pET28a-M8 were selected for reaction optimization. Key parameters—including expression temperature, inducer concentration, catalyst ratio, reaction temperature and pH, and concentrations of enzyme, prenol, Mg^{2+}, and DMSO—were systematically evaluated. Optimal conditions were determined to be: PCDF-MjIPK-EcPK: pET28a-M8 = 1:1, $OD_{600} = 120$, in 50 mM Tris-HCl buffer (pH 7.5), with 2 mM acceptor, 10 mM prenol, 2% DMSO (v/v), and incubation at 35 °C. Under these conditions, the reaction plateaued after 10 h, indicating efficient in situ DMAPP generation (Supplementary Figs. 25–27).

Following the success of DMAPP production, we extended this strategy to GPP biosynthesis from geraniol. Folk, a farnesol kinase from *Arabidopsis thaliana*, can also accept geraniol as a substrate[76], whereas THAIPK, an isopentenyl phosphate kinase from *Thermoplasma acidophilum*, naturally acts on DMAPP; however, engineered variant of THAIPKG (THAIPK-Y70A/V130A/I140A) is capable of accommodating geranyl phosphate (GP)[77]. Initially, the donor module PCDF-Folk-THAIPKG was constructed; however, poor expression and solubility of Folk in *E. coli*, even after N-terminal truncation (residues 1–65), hindered activity[73]. In contrast, we discovered by chance an assembled system comprising PCDF-THAIPKG and pET28a-M7 successfully catalyzed the formation of compound **6a**, albeit with a conversion of only 15.8%, which is significantly lower than the catalytic efficiency observed with the direct addition of GPP. Nevertheless, this result demonstrates the feasibility of an in situ GPP generation strategy from geraniol coupled with PT catalysis, enabling the production of geranylated products in whole-cell systems. With further optimization, such as enhancing GPP turnover efficiency, this platform could be extended to farnesol for in situ FPP generation and the subsequent biosynthesis of farnesylated products. Furthermore, application to substrates **1b** and **1 g** yielded corresponding geranylated products, confirming the effectiveness of this GPP generation system. Notably, replacing geraniol with its isomer nerol afforded **5b** and **4 g** with high efficiency, underscoring the system's substrate flexibility (Supplementary Fig. 31).

The versatility of the cascade platform was further validated across a range of flavonoid substrates. Considering both reaction activity and the synthetic value of the products-**2a** with anti-breast cancer activity[78], **2j** with anti-diabetic and neuroprotective effects[5,79], and analogs of **2 f** with antibacterial and cytotoxic activities[80,81], we selected substrates **1a, 1 f**, and **1j** for scale-up preparation. Preparative-scale reactions were performed for compounds **2a, 2 f**, and **2j** in 1 L systems, yielding 218 mg/L, 221 mg/L, and 442 mg/L of isolated products, respectively. An additional 11 products were synthesized in 50 mL reactions, each yielding between ~40–300 mg/L under optimized conditions (Fig. 6). These results highlight the broad applicability and scalability of the engineered prenylation platform, offering a robust and flexible strategy for the biosynthesis of structurally diverse prenylated flavonoids.

Discussion

In summary, we have successfully engineered three AtaPT variants—M8, G326W, and M7—that catalyze the regio- and chemoselective prenylation of flavonoids with markedly enhanced activity. Through a simultaneous multi-parameter directed evolution strategy, M8 emerged as the most efficient mutant, exhibiting a 45-fold increase in catalytic activity and a unique reverse 8-prenylation specificity toward kaempferol (**1a**) relative to the wild-type (WT) enzyme. While WT AtaPT shows a broad substrate scope, the engineered mutants exhibit enhanced substrate specificity toward flavonols, with significantly improved catalytic efficiencies and regioselectivities.

To elucidate the molecular basis underlying the enhanced catalytic performance, we determined the crystal structure of the M8 ternary complex with **1a** and DMSPP, the M7 binary complex with

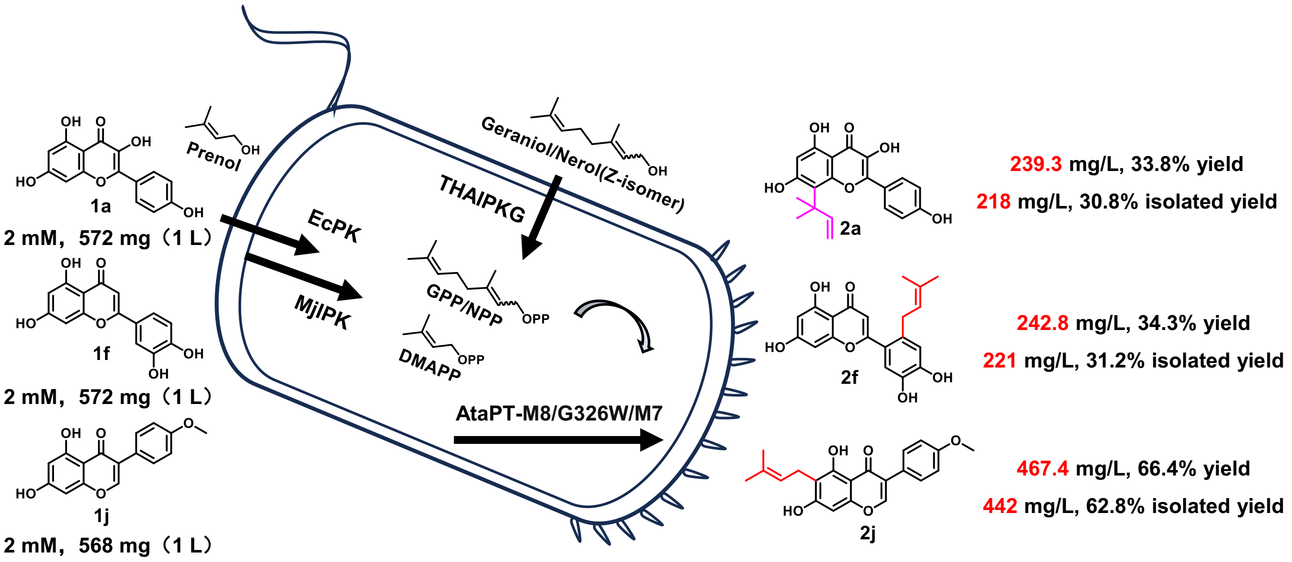

0.05 L Scale: 2i, 303.1 mg/L , 44.8%*; 3a, 40.1 mg/L , 5.7%*; 2e, 49.7 mg/L , 7.35%*; 2g, 375.4 mg/L , 55.2%*; 6a, 100.2 mg/L , 11.9%*; 3e, 53.6 mg/L , 6.6%*; 4i, 136.4 mg/L, 16.8%*; 4b, 210.6 mg/L , 24.1%* (Geraniol); 5b, 168.7 mg/L 19.3%* (Nerol); 3g, 219.3 mg/L 26.9%* (Geraniol); 4g, 181.8 mg/L , 22.3%* (Nerol).

Fig. 6 | Biocatalytic cascade reaction for prenylated flavonoid synthesis. The *E. coli* cells (harboring AtaPT-mutants or donor supply systems, 1:1 mixture) were resuspended in 50 mM Tris HCl buffer (pH 7.5), with the cell density adjusted to an OD_{600} of 120. After complete lysis, the reaction was carried out using the lysate. Substrates were added to the reaction mixture at final concentration of 2 mM receptor and 10 mM donor, in a total volume of either 1 L or 50 mL. Bioconversion reactions were performed at 35 °C, and 220 rpm for 24 h. M7: I167T/E169A/S170Q/S177G/L323Q/P324H/N328M and M8: I167A/E169A/S170Q/C175M/S177A/L323Q/P324H/N328R. THAIPKG: THAIPK-Y70A/V130A/I140A, * The yield was determined by converting the HPLC peak area using the corresponding standard calibration curve.

GSPP, resolved the structures of G326W, and performed molecular docking and molecular dynamics (MD) simulations. Structural analysis of M8 ternary complex revealed that key mutations—N328R, P324H, and C175M—reshaped the active site via newly formed hydrogen bonds and π-π interactions, stabilizing **1a** in a conformation favorable for C8 prenylation. Notably, the P324H mutation introduced an aromatic cage, which, in synergy with C175M, guided **1a** into the C8-selective binding pose. Furthermore, N328R played a dual role: it established a crucial hydrogen bond anchoring DMAPP in the central pocket, thereby defining donor specificity, and concurrently altered the DMAPP binding orientation, resulting in an enhanced activity.

In contrast, the absence of the C175M mutation and the substitution of N328R with N328M in M7 allowed the longer geranyl chain of GPP to be effectively accommodated within the aromatic cage formed by the P324H mutation. This structural configuration, together with a flexible loop (residues 167–170) acting as a potential gating element, enabled optimal positioning of the flavonoid substrate and facilitated highly selective B-ring or C3′-geranylation. In the G326W variant, the introduction of a bulky tryptophan residue disrupted the GPP-binding pocket present in the wild type, thereby preventing GPP acceptance. Nevertheless, G326W maintained a donor and acceptor-binding mode similar to that observed in M7, resulting in the same C3′ regioselectivity but a distinct donor specificity.

These mechanistic insights suggest that in prenyltransferases, regioselectivity is often tightly coupled to the identity and binding conformation of the prenyl donor. Therefore, in protein engineering efforts, the enzyme scaffold and prenyl donor should be considered as an integrated system. Alterations in the donor-binding site can profoundly influence not only donor specificity but also the chemo- and regioselectivity of the enzyme. Based on mechanistic insights, three homologous AtaPT enzymes were rationally engineered, each achieving substantial improvements in both activity and selectivity toward the deserved prenylated products. This further demonstrates that the aromatic cage mechanism observed in AtaPT is not unique and can be recapitulated in other homologous enzymes.

Leveraging these improvements, we demonstrated the synthetic utility of these enzymes by preparing 31 structurally diverse prenylated flavonoids—including flavonols, flavones, flavanones, and isoflavones—on a preparative scale. Additionally, we established a modular biocatalytic platform combining engineered prenyltransferases with in situ prenyl donor biosynthesis from prenol or geraniol. This cascade system enabled upscale production of 14 selected prenylated products with high efficiency and flexibility. Importantly, the developed approach enables the efficient bioproduction of prenylated flavonoids, thereby reducing reliance on large-scale plant cultivation and minimizing waste associated with traditional extraction methods that typically yield low product content. Moreover, the reactions are performed in aqueous media under mild temperature conditions, which decreases energy consumption and chemical waste, contributing to a more sustainable and environmentally friendly production process.

Altogether, this study presents a powerful strategy for constructing efficient and selective flavonoid prenyltransferases, deepens our understanding of their structure–function relationships, and provides a robust platform for the scalable biosynthesis of bioactive prenylated flavonoids.

Methods

Reagents and instruments

All chemical reagents were purchased from Aladdin, Macklin Biochemical, Meryer (Shanghai) Chemical Technology Co., 9ding Chemistry, Bide Pharm Tech, Shanghai Yuan Ye Biotechnology Co., or Sangon Biotech (Shanghai, China) unless otherwise stated. The KOD One TM PCR master Mix polymerase was obtained from Toyobo Ideas & Chemistry. *Dpn*I was purchased from Abclonal Technology. The ClonExpress MultiS One-Step Cloning Kit was obtained from Vazyme Biotech. Primer synthesis and DNA sequencing were conducted at Sangon Biotech Company (Shanghai, China). Microspectrophotometer (Allsheng, Nano-300), ultrasonic homogenizer with noise isolating chamber (SCIENTZ-IID), freeze drier (SCIENTZ-10ND), centrifuge (Thermo Fisher, (Sorvall ST 16 R) and PICO 17), PCR Amplifier (BIO-RAD, T100^{TM} Thermal Cycler), mini shaker (Allsheng, MSC-100), shaker (Minquan, MQD-BIR). Shimadzu Nexis LC 20AT equipped with an electrospray ionization (ESI) source was used for the measurement of substrates and products. High resolution mass spectrometry (HRMS) detection was performed by X500R QTOF from AB SCIEX. The prenylated products were isolated and purified by semi-preparative HPLC on an LC-8A instrument (Shimadzu). Products were characterized by ^{1}HNMR and ^{13}C NMR in DMSO-d_6 on AV2 500 MHz Bruker spectrometer. Chemical shifts (δ) were given in ppm and coupling constants (J) were given in hertz (Hz).

Heterogonous expression and purification of PTs

AtaPT DNA sequence were synthesized by GENEWIZ(China), and then inserted into the *Nde*I-*Xho*I site of pET28a. The recombinant plasmid pET28a-AtaPT were transformed into *E. coli* BL21(DE3) for heterologous expression. *E. coli* cells were cultured (5 mL) overnight in Luria-Bertani (LB) medium containing 50 μg/mL kanamycin at 37 °C with shaking (220 rpm). Subsequently, 1% seeding cultures were transferred into 500 mL TB-medium containing 50 μg/mL of kanamycin and grown at 37 °C and 220 rpm in 2 L shake flasks. After the OD$_{600}$ reached 0.8–1.0, the expression of recombinant AtaPT were induced with 0.2 mM IPTG at 18 °C, 220 rpm for 16 h. The cells were harvested by centrifugation at 6,438 g for 3 min at 4 °C and then resuspended in binding buffer (50 mM Tris-HCl, 5 mM CaCl$_2$, pH 7.5)[49,50]. After cell rupture by sonication in ice bath, the cell debris was removed by centrifugation at 15,480 g and 4 °C for 1 h. The soluble fraction was passed through a 0.45 μm syringe filter. The supernatant was applied to an ÄKTA avant 25 system equipped with a 5-mL HisTrap^{TM} HP column following the manufacturer's instructions, using a linear gradient of 10-500 mM imidazole in 50 mM Tris-HCl, 5 mM CaCl$_2$, pH 7.5 (Supplementary Fig. 12).

Construction and screening of AtaPT mutant libraries

All strains, plasmids, and primers used in this study are listed in Supplementary Tables 2 and 3. PCR assays (Supplementary Table 4) were conducted with KOD One^{TM} PCR master Mix. Following sequence verification, the recombinant plasmids were transformed into *E. coli* BL21 (DE3) for heterologous protein expression, as described above. Single-site saturation mutagenesis (SSM) and iterative saturation mutagenesis (ISM) was performed using primers containing NNK codons at targeted sites. To ensure adequate library coverage, 92 colonies were screened per mutagenized site. Colonies were cultured in 96-deep-well plates containing 0.3 mL LB medium supplemented with 50 μg/mL kanamycin at 37 °C overnight. Subsequently, 0.7 mL TB medium containing 50 μg/mL kanamycin and 0.2 mM IPTG was added, and cultures were incubated at 18 °C for 16 h. Cells were harvested and resuspended in 0.2 mL reaction buffer (2 mM substrate **1a**, 2 mM DMAPP, 50 mM Tris-HCl, 5 mM CaCl$_2$, pH 7.5) and incubated at 37 °C for 24 h with shaking. Reactions were quenched by the addition of 0.6 mL methanol. Relative activity was determined by whole-cell biotransformation in a total volume of 2 mL reaction buffer (2 mM **1a**, 2 mM DMAPP, 50 mM Tris-HCl, 5 mM CaCl$_2$, pH 7.5) at 37 °C for 24 h, using the wild-type enzyme as a control. Samples were centrifuged at 12,000 g for 15 min and analyzed by HPLC/UV using a SHIMADZU Shim-pack GIS C18 column (4.6 × 250 mm, 5 μm) at a flow rate of 1 mL/min and column temperature of 30 °C. The gradient elution programs are detailed in Supplementary Table 5.

Determination of kinetic parameters

Kinetic analyses were conducted for AtaPT-M8 and AtaPT-G326W using DMAPP, and for AtaPT-WT and AtaPT-M7 using GPP, with **1a** as the substrate. Enzymatic assays were performed in 100 μL reaction volumes containing 50 mM Tris-HCl buffer (pH 7.5), 5 mM CaCl$_2$, 2/5/10 μM enzyme, 2 or 4 mM saturated DMAPP/GPP, and varying concentrations of **1a** (40, 60, 80, 100, 150, 200, 250, 300, 500, 1000, 1500, 2000, 2500, and 4000 μM). Reactions were incubated at 37 °C for 10 or 20 min, then quenched by the addition of 300 μL methanol and centrifuged at 13,800 g for 15 min. Supernatants were analyzed by HPLC as previously described.

All experiments were performed in triplicate. Michaelis–Menten constants (K_m) were determined by non-linear regression fitting, and turnover numbers (k_{cat}) were calculated accordingly (Supplementary Table 9 and Supplementary Fig. 13).

Structure determination of AtaPT mutants

The AtaPT variants (M8, G326W, S177G, and M7(11–424)), each bearing an N-terminal 6×His tag, were overexpressed in *E. coli* BL21(DE3) cells. Protein expression was induced with 0.4 mM IPTG when cultures reached an OD$_{600}$ of 0.8, followed by incubation at 16 °C for 12 h. Cells were harvested and lysed in lysis buffer containing 25 mM Tris-HCl (pH 8.0), 1 M NaCl, 25 mM imidazole, 0.5 mM *β*-mercaptoethanol (*β*-ME), and 1 mM phenylmethylsulfonyl fluoride (PMSF). The His-tagged fusion proteins were purified using Ni^{2+}-affinity chromatography. The column was washed with buffer containing 25 mM Tris-HCl (pH 8.0), 25 mM imidazole, and 1 M NaCl, and proteins were eluted with 250 mM imidazole in the same buffer. Further purification was performed by size-exclusion chromatography using a Superdex 75 column (GE Healthcare) pre-equilibrated with buffer containing 25 mM Bis-Tris (pH 6.5), 200 mM NaCl, 5% (v/v) glycerol, and 3 mM dithiothreitol (DTT). The purified proteins were concentrated to 25 mg/mL and stored at −80 °C. The small molecule 1a was dissolved in DMSO to a final concentration of 100 mM. Crystallization was performed using the hanging-drop vapor diffusion method at 20 °C. Equal volumes (1 μL each) of protein-ligand complex solution and reservoir buffer were mixed and equilibrated against 500 μL of reservoir solution. Crystals were obtained in a buffer containing 0.1 M Bis-Tris (pH 6.5), 0.2 M ammonium sulfate, and 20% (w/v) PEG 3350, typically reaching full size within ~5 days. The crystals were then soaked with **1a** (20 mM) and analogues of prenyl donors (DMSPP or GSPP, 10 mM) for 5 min to 12 h. Prior to flash-freezing in liquid nitrogen, crystals were cryoprotected using the reservoir buffer supplemented with 20% (v/v) glycerol. X-ray diffraction data were collected at beamline BL19U1 of the Shanghai Synchrotron Radiation Facility and BL02U1 at Shanghai Synchrotron Radiation Facility. Data were indexed, integrated, and scaled using the HKL3000 software package[82]. The structures were solved by molecular replacement using PHASER[83] with the structure of AtaPT-WT (PDB: 5KCG) as the searching model. Following iterative manual rebuilding and refinement were performed with the use of COOT[84] and PHENIX[85], respectively.

Reaction condition optimization

All optimization experiments were performed in triplicate on an analytical scale (300 μL) using whole-cell catalysts, with DMAPP as the prenyl donor and **1a** as the acceptor. Reaction conditions—37 °C, 50 mM Tris-HCl (pH 7.5), and 5 mM CaCl$_2$—were based on previously reported protocols. specifically at 37 °C, 50 mM Tris-HCl (pH 7.5), and 5 mM CaCl$_2$. To evaluate the effect of the co-solvent DMSO, reactions were carried out under optimized conditions with varying DMSO concentrations (2%, 4%, 6%, 8%, and 10% v/v) (Supplementary Fig. 10). The influence of cell density on product formation (**2a, 3a**, and **6a**) was assessed by conducting reactions at different OD$_{600}$ values (40, 60, 80, 100, and 120) in 50 mM Tris-HCl buffer (pH 7.5). Product titers increased with cell density up to an OD$_{600}$ of 80, after which a decline was observed at OD$_{600}$ = 100. To investigate the effect of reaction time, biotransformations were carried out at 37 °C in 50 mM Tris-HCl buffer (pH 7.5) containing 6% (v/v) DMSO. Reactions were sampled at various time points (2, 4, 6, 8, 10, 12, and 24 h). Reactions were quenched by the addition of 0.9 mL methanol, and supernatants were analyzed by analytical HPLC as described previously (Supplementary Table 5 and Supplementary Fig. 10).

Preparation of *E. coli* whole cell catalyst harboring AtaPT mutants

After protein expression, the cells were harvested by centrifugation at 6438 g for 2 min at 4 °C, then resuspended in binding buffer (50 mM Tris-HCl, 5 mM $CaCl_2$, pH = 7.5) at $OD_{600} = 80$. The wet pellets were stored at -80 °C until further use.

HPLC-ESI and HRMS-based prenyltransferase activity assay

For the in vitro activity assay, the reaction mixture contained 4 mM DMAPP or GPP, 2 mM acceptor substrate, 6% (v/v) DMSO, and whole cell ($OD_{600} = 80$) in a total volume of 300 μL of 50 mM Tris-HCl buffer (pH 7.5) supplemented with 5 mM $CaCl_2$. Reactions were incubated at 37 °C for 8 or 12 h and quenched by addition of 900 μL methanol. After centrifugation at 13,800 g for 15 min, the supernatants were analyzed by HPLC-ESI and high-resolution mass spectrometry (HRMS). All reactions were performed in triplicate. Gradient programs used for analysis are detailed in Supplementary Table 5 and Supplementary Figs. 32-54. For the substrate scope experiments, conversion rates were determined from the ratio of the product peak area to the substrate peak area in HPLC.

Product identification by NMR

Recombinant *E. coli* strains harboring pET28a-AtaPT-M8, pET28a-AtaPT-G326W, pET28a-AtaPT-S177G, or pET28a-AtaPT-M7 were prepared and induced as described above. After induction, the whole cells were harvested by centrifugation and washed with 50 mM Tris-HCl buffer (pH 7.5) containing 5 mM $CaCl_2$. The cells were then resuspended in the same buffer, and the optical density was adjusted to $OD_{600} = 80$. The reaction mixture (total volume: 50 mL in a 250 mL Erlenmeyer flask) was prepared by adding 2 mM acceptor substrate and 4 mM DMAPP or GPP. Bioconversion was carried out at 37 °C with shaking for 8-12 h. After the reaction, the mixture was extracted with an equal volume of ethyl acetate and centrifuged at 6438 g for 10 min. The supernatant was collected and transferred to a separating funnel, where the aqueous phase was discarded, and the organic phase was retained. The solvent was removed under reduced pressure, and the resulting residue was dissolved in methanol and purified by reverse-phase semi-preparative HPLC. The purified products were dissolved in DMSO-d_6 and characterized by ^1H and ^{13}C NMR spectroscopy (Supplementary Figs. 24, 55–119).

Molecular docking and Molecular dynamics (MD) simulations

Molecular docking of compound **1a** and GPP into the M7 variant was conducted using the Glide module Schrödinger, LLC, New York, NY, 2024) in Standard Precision (SP) mode. Prior to docking, the M7 structure was prepared by optimizing the hydrogen bond network, removing water molecules, and energy minimization in Protein Preparation Wizard. Compound **1a** and GPP were prepared using Ligprep. A receptor grid box centered on the active site was generated using the Receptor Grid Generation module. The docking poses consistent with in vitro enzymatic assay results were selected for molecular dynamics (MD) simulations.

MD simulations were carried out using the Desmond. The protein-ligand complexes were solvated in an SPC water model, and the systems were neutralized with 0.15 M NaCl. All simulations employed the OPLS4 force field, with the default cutoff values used for Coulombic interactions. Following energy minimization, the systems were equilibrated using both NVT and NPT ensembles. Subsequently, production runs were performed for 250 ns at 300 K and 1 atm. And Simulation Interactions Diagram was employed to evaluate the stability and binding interactions of the ligand-protein complexes.

Construction and characterization of other PTs mutants

Using AtaPT as a template for BLAST searches against the NCBI database, three homologous enzymes with distinct degrees of sequence identity were selected: AfaPT (94.81%, NCBI GenBank: KAL5359867.1), AaaPT (86.7%, NCBI GenBank: XP_073546247.1), and AmaPT (56.87%, NCBI GenBank: XP_045942482.1). The DNA sequences of AfaPT, AaaPT, and AmaPT were synthesized by General Biosystems (Anhui) Corp. Ltd and cloned into the *Nde*I–*Xho*I sites of the pET28a vector. The resulting recombinant plasmids (pET28a-AfaPT, pET28a-AaaPT, and pET28a-AmaPT) were transformed into Escherichia coli BL21(DE3) for heterologous expression.

E. coli cells were cultured overnight in 5 mL of Luria–Bertani (LB) medium supplemented with 50 μg/mL kanamycin at 37 °C with shaking at 220 rpm. The overnight cultures were then inoculated (1%, v/v) into 500 mL of TB medium containing 50 μg/mL kanamycin and grown at 37 °C and 220 rpm in 2 L shake flasks. When the OD_{600} reached 0.8–1.0, recombinant protein expression was induced with 0.2 mM IPTG, followed by incubation at 18 °C and 220 rpm for 16 h. Engineered mutants of the PT homologs were constructed by PCR using KOD One™ PCR Master Mix.

Whole-cell biotransformation assays were performed in a final volume of 0.3 mL containing 50 mM Tris–HCl buffer (pH 7.5), 5 mM $CaCl_2$, 4 mM DMAPP or GPP, 2 mM acceptor substrate **1a**, 6% (v/v) DMSO, and enzyme preparations adjusted to an OD_{600} of 80. Reactions were conducted at 37 °C for 8 h and terminated by the addition of 0.9 mL methanol. After centrifugation at 13,800 × *g* for 15 min, the supernatants were subjected to HPLC analysis. All experiments were performed in triplicate ($n = 3$).

Coupling of IUP with AtaPT-M8/G326W/M7 for the preparation of prenylflavonoids using a lysate-based catalyst

The cascade biosynthesis of prenylflavonoids was optimized using mixed whole-cell lysates of *E. coli* BL21(DE3) harboring pET28a-M8 and PCDF-MjIPK-EcPK[74], with substrate **1a**. The influence of various parameters was investigated, including expression temperature (18, 25, 30, or 37 °C), IPTG concentration (0.2, 0.5, 0.8, or 1 mM), reaction temperature and pH (18, 25, 30, or 37 °C; pH 7.0, 7.5, 8.0, 8.5, or 9.0), enzyme lysate ratio (PCDF-MjIPK-EcPK: pET28a-M8 = 1: 3, 1: 2, 1: 1, 2: 1, or 3: 1), DMSO content (1-10% v/v), Mg^{2+} concentration (0, 2, 5, or 10 mM), prenol concentration (2–30 mM), and cell density ($OD_{600} = 40\text{-}200$). The reaction reached a steady state after approximately 10 h. Reactions were terminated by adding three volumes of methanol, followed by centrifugation at 13,800 g for 15 min. Products were analyzed by HPLC, and all concentrations are reported as mean ± SD from three biological replicates (Supplementary Figs. 25–27).

For strain cultivation, *E. coli* harboring the relevant plasmids was grown in TB medium containing 50 μg/mL kanamycin or 100 μg/mL spectinomycin at 37 °C until OD_{600} reached 0.8–1.0. IPTG (0.2 or 0.5 mM) was added to induce expression, followed by incubation at 18 or 25 °C for 16 h. To enable large-scale production, a high-density fermentation method was also established using glucose as a carbon source. This process is cost-effective and enables high cell density (Supplementary Table 13). Cultures were grown at 37 °C until OD_{600} reached 25-30, followed by induction with 1 mM IPTG and continued expression overnight at 18 or 25 °C. During induction, glucose levels were maintained between 0.5–2 g/L until its consumption ceased. Cells were harvested by centrifugation at 6438 g for 2 min at 4 °C and resuspended in 50 mM Tris-HCl buffer (pH 7.5) to an OD_{600} of 120.

The cascade preparation of alkylated flavonoids was conducted with 2 mM of substrates **1a, 1 f**, or **1j**, 10 mM prenol, and 2% DMSO in a total volume of 1 L. The reaction was carried out at 35 °C for 10 h.

Afterward, samples were extracted with two volumes of ethyl acetate and centrifuged at 6438 g for 5 min. The supernatants were collected and the solvents evaporated under reduced pressure. The residues were dissolved in dichloromethane (DCM) and purified via silica gel chromatography (DCM: MeOH = 30: 1). The eluates were concentrated under reduced pressure to obtain the final products, which were subsequently dried.

Additionally, substrates were evaluated using pET28a-G326W and PCDF-MjIPK-EcPK, or pET28a-M7 combined with pET28a-THAIPK-Y70A/V130A/I140A (referred to as THAIPKG)[77]. The G326W combination exhibited higher reactivity toward **1a, 1e**, and **1 g**, while the M7-THAIPKG system showed enhanced activity for **1a, 1b, 1e, 1 g**, and **1i**, particularly in aromatic geranylation. Interestingly, replacing geraniol with nerol in reactions with substrates **1b** and **1 g** resulted in notable activity, an unexpected yet intriguing outcome. The yield was determined by substituting the peak area into the standard calibration curve.

Reporting summary

Further information on research design is available in the Nature Portfolio Reporting Summary linked to this article.

Data availability

The atomic coordinates and structure factors of AtaPT mutants have been deposited in the Protein Data Bank under the codes 9V3U for AtaPT-M7, 9V5G for AtaPT-M8 and 9V5F for AtaPT-G326W, respectively. Three prenyltransferases were retrieved from the database, and their GenBank accession codes are KAL5359867.1 (AfaPT), XP_073546247.1 (AaaPT), XP_045942482.1 (AmaPT). The source data for the molecular dynamic simulations are available at the following address: https://zenodo.org/records/17983856. Source data are provided with this paper. All data supporting the findings of this study are available within the article, its supplementary information files and from the corresponding authors upon request. Source data are provided with this paper.

References

1. Hanáková, Z. et al. *C*-geranylated flavanones from paulownia tomentosa fruits as potential anti-inflammatory compounds acting via inhibition of TNF-α production. *J. Nat. Prod.* **78**, 850–863 (2015).
2. Osorio, M. et al. Prenylated flavonoids with potential antimicrobial activity: synthesis, biological activity, and in silico study. *Int. J. Mol. Sci.* **22**, 5472 (2021).
3. Santos, C. M. M. & Silva, A. M. S. The antioxidant activity of prenylflavonoids. *Molecules* **25**, 696 (2020).
4. Molčanová, L., Janošíková, D., Dall´Acqua, S. & Šmejkal, K. *C*-prenylated flavonoids with potential cytotoxic activity against solid tumor cell lines. *Phytochem. Rev.* **18**, 1051–1100 (2019).
5. Jo, Y. H. et al. Anti-diabetic potential of *Masclura tricuspidata* leaves: prenylated isoflavonoids with α-glucosidase inhibitory and anti-glycation activity. *Bioorg. Chem.* **114**, 105098 (2021).
6. Guo, Y.-Q. et al. Prenylated flavonoids as potent phosphodiesterase-4 inhibitors from *Morus alba*: isolation, modification, and structure-activity relationship study. *Eur. J. Med. Chem.* **144**, 758–766 (2018).
7. Shi, S., Li, J., Zhao, X., Liu, Q. & Song, S.-J. A comprehensive review: Biological activity, modification and synthetic methodologies of prenylated flavonoids. *Phytochemistry* **191**, 105098 (2021).
8. Lv, H.-W. et al. Phytochemistry and pharmacology of natural prenylated flavonoids. *Arch. Pharm. Res.* **46**, 207–272 (2023).
9. Nguyen, G.-N., Jordan, E. N. & Kayser, O. Synthetic strategies for rare cannabinoids derived from *Cannabis sativa*. *J. Nat. Prod.* **85**, 1555–1568 (2022).
10. Matsumoto, T., Fujimoto, Y., Watabe, Y., Yanai, H. & Taguchi, T. An efficient isoprenylation of xanthones at the C1 position by utilizing anion-accelerated aromatic oxy-cope rearrangement. *Synlett* **27**, 848–853 (2016).
11. Hu, Y.-C., Min, X.-T., Ji, D.-W. & Chen, Q.-A. Catalytic prenylation and reverse prenylation of aromatics. *Trends Chem.* **4**, 658–675 (2022).
12. Wang, Y. et al. Directed evolution: methodologies and applications. *Chem. Rev.* **121**, 12384–12444 (2021).
13. Reetz, M. Making enzymes suitable for organic chemistry by rational protein design. *ChemBioChem* **23**, e202200049 (2022).
14. Reetz, M. T. Laboratory evolution of stereoselective enzymes: a prolific source of catalysts for asymmetric reactions. *Angew. Chem., Int. Ed.* **50**, 138–174 (2010).
15. Turner, N. J. Directed evolution drives the next generation of biocatalysts. *Nat. Chem. Biol.* **5**, 567–573 (2009).
16. Zeymer, C. & Hilvert, D. Directed evolution of protein catalysts. *Annu. Rev. Biochem.* **87**, 131–157 (2018).
17. Arnold, F. H. Innovation by evolution: bringing new chemistry to life (Nobel Lecture). *Angew. Chem., Int. Ed.* **58**, 14420–14426 (2019).
18. Li, M. et al. An efficient *C*-glycoside production platform enabled by rationally tuning the chemoselectivity of glycosyltransferases. *Nat. Commun.* **15**, 8893 (2024).
19. Lim, K. J. H. et al. Structure-guided engineering of prenyltransferase NphB for high-yield and regioselective cannabinoid production. *ACS Catal.* **12**, 4628–4639 (2022).
20. Kille, S., Zilly, F. E., Acevedo, J. P. & Reetz, M. T. Regio- and stereoselectivity of P450-catalysed hydroxylation of steroids controlled by laboratory evolution. *Nat. Chem.* **3**, 738–743 (2011).
21. An, T., Feng, X. & Li, C. Prenylation: a critical step for biomanufacturing of prenylated aromatic natural products. *J. Agric. Food Chem.* **71**, 2211–2233 (2023).
22. Mori, T. Enzymatic studies on aromatic prenyltransferases. *J. Nat. Med.* **74**, 501–512 (2020).
23. Miller, E. T., Tsodikov, O. legV. & Garneau-Tsodikova, S. Structural insights into the diverse prenylating capabilities of DMATS prenyltransferases. *Nat. Prod. Rep.* **41**, 113–147 (2024).
24. Chen, H.-P. & Abe, I. Microbial soluble aromatic prenyltransferases for engineered biosynthesis. *Synth. Syst. Biotechol.* **6**, 51–62 (2021).
25. Sasaki, K., Mito, K., Ohara, K., Yamamoto, H. & Yazaki, K. Cloning and characterization of naringenin 8-prenyltransferase, a flavonoid-specific prenyltransferase of *Sophora flavescens*. *Plant Physiol.* **146**, 1075–1084 (2008).
26. Sasaki, K., Tsurumaru, Y., Yamamoto, H. & Yazaki, K. Molecular characterization of a membrane-bound prenyltransferase specific for isoflavone from *Sophora flavescens*. *J. Biol. Chem.* **286**, 24125–24134 (2011).
27. Chen, R. et al. Regio- and stereospecific prenylation of flavonoids by *Sophora flavescens* prenyltransferase. *Adv. Synth. Catal.* **355**, 1817–1828 (2013).
28. Li, J. et al. GuA6DT, a regiospecific prenyltransferase from glycyrrhiza uralensis, catalyzes the 6-prenylation of flavones. *ChemBioChem* **15**, 1673–1681 (2014).
29. Li, J. et al. Biocatalytic access to diverse prenylflavonoids by combining a regiospecific *C*-prenyltransferase and a stereospecific chalcone isomerase. *Acta Pharm. Sin. B* **8**, 678–686 (2018).
30. Shen, G. et al. Characterization of an isoflavonoid-specific prenyltransferase from *Lupinus albus*. *Plant Physiol.* **159**, 70–80 (2012).
31. Liu, J., Xia, Y., Jiang, W., Shen, G. & Pang, Y. LaPT2 gene encodes a flavonoid prenyltransferase in *White Lupin*. *Front. Plant Sci.* **12**, 673337 (2021).
32. Rea, K. A. et al. Biosynthesis of cannflavins A and B from *Cannabis sativa* L. *Phytochemistry* **164**, 162–171 (2019).
33. Shen, G. et al. The discovery of a key prenyltransferase gene assisted by a chromosome-level *Epimedium pubescens* genome. *Front. Plant Sci.* **13**, 1034943 (2022).
34. Parker, E. J. et al. Structural basis for non-genuine phenolic acceptor substrate specificity of *Streptomyces roseochromogenes*

prenyltransferase CloQ from the ABBA/PT-barrel superfamily. *Plos One* **12**, 1034943 (2017).

35. Ozaki, T., Mishima, S., Nishiyama, M. & Kuzuyama, T. NovQ is a prenyltransferase capable of catalyzing the addition of a dimethylallyl group to both phenylpropanoids and flavonoids. *J. Antibiot.* **62**, 385–392 (2009).
36. Kumano, T., Richard, S. B., Noel, J. P., Nishiyama, M. & Kuzuyama, T. Chemoenzymatic syntheses of prenylated aromatic small molecules using *Streptomyces* prenyltransferases with relaxed substrate specificities. *Bioorg. Med. Chem.* **16**, 8117–8126 (2008).
37. Yu, X. & Li, S. M. Prenylation of flavonoids by using a dimethylallyltryptophan synthase, 7-DMATS, from *Aspergillus fumigatus*. *ChemBioChem* **12**, 2280–2283 (2011).
38. Zhou, K., Yu, X., Xie, X. & Li, S.-M. Complementary flavonoid prenylations by fungal indole prenyltransferases. *J. Nat. Prod.* **78**, 2229–2235 (2015).
39. Liu, Y. et al. Understanding and engineering of *C*4 indole prenyltransferase FgaPT2 by theoretical study and mutation experiments. *ACS Catal.* **15**, 4921–4933 (2025).
40. Chen, X.-W., Liu, Z., Dai, S. & Zou, Y. Discovery, characterization and engineering of the free L-histidine *C*4-prenyltransferase. *J. Am. Chem. Soc.* **146**, 23686–23691 (2024).
41. Wang, W. et al. Characterization and structural analysis of a versatile aromatic prenyltransferase for imidazole-containing diketopiperazines. *Nat. Commun.* **16**, 144 (2025).
42. Zhao, W. et al. Mutation on Gly115 and Tyr205 of the cyclic dipeptide *C*2-prenyltransferase FtmPT1 increases its catalytic activity toward hydroxynaphthalenes. *Appl. Microbiol. Biotechnol.* **101**, 1989–1998 (2016).
43. Xu, Y. et al. Dearomative gem-diprenylation of hydroxynaphthalenes by an engineered fungal prenyltransferase. *RSC Adv.* **12**, 27550–27554 (2022).
44. Martin, A., Dierlamm, N., Zocher, G. & Li, S.-M. A basidomycetous hydroxynaphthalene-prenylating enzyme exhibits promiscuity toward prenyl donors. *Appl. Microbiol. Biotechnol.* **107**, 4845–4852 (2023).
45. Tanaya, R. et al. Catalytic potential of *Cannabis* prenyltransferase to expand cannabinoid scaffold diversity. *Org. Lett.* **25**, 8601–8605 (2023).
46. Ostertag, E. et al. Reprogramming substrate and catalytic promiscuity of tryptophan prenyltransferases. *J. Mol. Biol.* **433**, 166726 (2021).
47. Yang, Y. et al. Fungal prenyltransferase AnaPT and its F265 mutants catalyze the dimethylallylation at the nonaromatic carbon of phloretin. *J. Agric. Food Chem.* **72**, 8018–8026 (2024).
48. Chen, R. et al. Molecular insights into the enzyme promiscuity of an aromatic prenyltransferase. *Nat. Chem. Biol.* **13**, 226–234 (2016).
49. Ran, Q. et al. Geranylation of chalcones by a fungal aromatic prenyltransferase. *J. Agric. Food Chem.* **71**, 4675–4682 (2023).
50. Wu, Y. et al. Increasing structure diversity of farnesylated chalcones by a fungal aromatic prenyltransferase. *Phytochemistry* **224**, 114149 (2024).
51. Wang, P. et al. Complete biosynthesis of the potential medicine icaritin by engineered *Saccharomyces cerevisiae* and *Escherichia coli*. *Sci. Bull.* **66**, 1906–1916 (2021).
52. An, T. et al. De novo biosynthesis of anticarcinogenic icariin in engineered yeast. *Metab. Eng.* **80**, 207–215 (2023).
53. Feng, K.-P. et al. Enzymatic synthesis of anhydroicaritin, baohuoside and icariin. *J. Asian Nat. Prod. Res.* **25**, 667–673 (2022).
54. Sun, W.-Z. et al. Metabolic engineering of *Yarrowia lipolytica* for enhanced de novo biosynthesis of icaritin. *ACS Synth. Biol.* **14**, 1142–1151 (2025).
55. Acevedo-Rocha, C. G. et al. Directed evolution of proteins based on mutational scanning. *Methods Mol. Biol.* **1685**, 87–128 (2018).
56. Reetz, M. T. & Carballeira, J. D. Iterative saturation mutagenesis (ISM) for rapid directed evolution of functional enzymes. *Nat. Protoc.* **2**, 891–903 (2007).
57. Reetz, M. T., Carballeira, J. D. & Vogel, A. Iterative saturation mutagenesis on the basis of B factors as a strategy for increasing protein thermostability. *Angew. Chem. Int. Ed.* **118**, 7909–7915 (2006).
58. Parra, L. P., Agudo, R. & Reetz, M. T. Directed evolution by using iterative saturation mutagenesis based on multiresidue sites. *ChemBioChem* **14**, 2301–2309 (2013).
59. Hollmann, F., Sanchis, J. & Reetz, M. T. Learning from protein engineering by deconvolution of multi-mutational variants. *Angew. Chem. Int. Ed.* **63**, e202404880 (2024).
60. Li, D., Wu, Q. & Reetz, M. T. Focused rational iterative site-specific mutagenesis (FRISM). *Method. Enzymol.* **643**, 225–242 (2020).
61. Qu, G., Li, A., Acevedo-Rocha, C. G., Sun, Z. & Reetz, M. T. The crucial role of methodology development in directed evolution of selective enzymes. *Angew. Chem. Int. Ed.* **59**, 13204–13231 (2020).
62. Bao, Y., Xu, Y. & Huang, X. Focused rational iterative site-specific mutagenesis (FRISM): a powerful method for enzyme engineering. *Mol. Catal.* **553**, 113755 (2024).
63. Reetz, M. T. A breakthrough in protein engineering of a glycosyltransferase. *Green. Synth. Catal.* **2**, 4–5 (2021).
64. Mou, K. et al. Stereodivergent protein engineering of fatty acid photodecarboxylase for light-driven kinetic resolution of sec-alcohol oxalates. *Angew. Chem. Int. Ed.* **63**, e202318374 (2024).
65. Yang, C. et al. Synergy between methylerythritol phosphate pathway and mevalonate pathway for isoprene production in *Escherichia coli*. *Metab. Eng.* **37**, 79–91 (2016).
66. Chatzivasileiou, A. O., Ward, V., Edgar, S. M. & Stephanopoulos, G. Two-step pathway for isoprenoid synthesis. *Proc. Natl. Acad. Sci.* **116**, 506–511 (2018).
67. Levisson, M. et al. Toward developing a yeast cell factory for the production of prenylated flavonoids. *J. Agric. Food Chem.* **67**, 13478–13486 (2019).
68. Yang, S., Chen, R., Cao, X., Wang, G. & Zhou, Y. J. De novo biosynthesis of the hops bioactive flavonoid xanthohumol in yeast. *Nat. Commun.* **15**, 253 (2024).
69. Qiu, C., Liu, Y., Wu, Y., Zhao, L. & Pei, J. Biochemical characterization of a novel prenyltransferase from *Streptomyces sp. NT11* and development of a recombinant strain for the production of 6-prenylnaringenin. *J. Agric. Food Chem.* **69**, 14231–14240 (2021).
70. Liu, Y., Wu, Y., Zhao, L. & Pei, J. Regiospecific 3′-*C*-prenylation of naringenin by *Nocardiopsis gilva* prenyltransferase. *Enzyme Microb. Technol.* **163**, (2023).
71. Zhang, X. et al. Coupling the isopentenol utilization pathway and prenyltransferase for the biosynthesis of licoflavanone in recombinant *Escherichia coli*. *J. Agric. Food Chem.* **72**, 15832–15840 (2024).
72. Fan, Z. et al. Heterologous biosynthesis of prenylflavonoids in *Escherichia coli* based on fungus screening of prenyltransferases. *ACS Omega* **10**, 8891–8900 (2025).
73. Wang, L. et al. Systematic biotechnological production of isoprenoid analogs with bespoke carbon skeletons. *Nat. Commun.* **16**, 2098 (2025).
74. Johnson, L. A., Dunbabin, A., Benton, J. C. R., Mart, R. J. & Allemann, R. K. Modular chemoenzymatic synthesis of terpenes and their analogues. *Angew. Chem. Int. Ed.* **59**, 8486–8490 (2020).
75. Qiu, C., Liu, Y., Wu, Y., Zhao, L. & Pei, J. Functional characterization and screening of promiscuous kinases and isopentenyl phosphate kinases for the synthesis of DMAPP via a one-pot enzymatic cascade. *Int. J. Mol. Sci.* **23**, 12904 (2022).
76. Fitzpatrick, A. H., Bhandari, J. & Crowell, D. N. Farnesol kinase is involved in farnesol metabolism, ABA signaling and flower development in *Arabidopsis*. *Plant J.* **66**, 1078–1088 (2011).

77. Mabanglo, M. F., Pan, J.-J., Shakya, B. & Poulter, C. D. Mutagenesis of isopentenyl phosphate kinase to enhance geranyl phosphate kinase activity. *ACS Chem. Biol.* **7**, 1241–1246 (2012).
78. Thai, Q. D. et al. Phytochemical Study and Biological Evaluation of Chemical Constituents of *Platanus Orientalis* and *Platanus × Acerifolia Buds*. *Phytochemistry* **130**, 170–181 (2016).
79. Hiep, N. T. et al. Isoflavones with Neuroprotective Activities from Fruits of *Cudrania Tricuspidata*. *Phytochemistry* **111**, 141–148 (2015).
80. Zhang, H. et al. Flavonoids from the Leaves of Epimedium *Koreanum Nakai* and Their Potential Cytotoxic Activities. *Nat. Prod. Res.* **34**, 1256–1263 (2019).
81. Zhu, W. et al. Cytotoxic Phenolic Constituents from *Hypericum japonicum*. *Phytochemistry* **164**, 33–40 (2019).
82. Minor, W., Cymborowski, M., Otwinowski, Z. & Chruszcz, M. HKL-3000: the integration of data reduction and structure solution–from diffraction images to an initial model in minutes. *Acta Crystallogr. D. Biol. Crystallogr.* **62**, 859–866 (2006).
83. McCoy, A. J. et al. Phasercrystallographic software. *J. Appl. Crystallogr.* **40**, 658–674 (2007).
84. Emsley, P. & Cowtan, K. Coot: model-building tools for molecular graphics. *Acta Crystallogr. D. Biol. Crystallogr.* **60**, 2126–2132 (2004).
85. Paul, D. A. et al. Coot: model-building tools for molecular graphics. *Acta Crystallogr. D. Biol. Crystallogr.* **60**, 2126–2132 (2004).

Acknowledgements

J.W. and M.C. acknowledge the financial support from the National Key Research and Development Program of China (No. 2023YFA0914100/2023YFA0914102), J. W. thank the funding from the National Natural Science Foundation of China (22477110 and 22034002), and the Fundamental Research Funds for the Central Universities (226202400061 and 226202300100). Z.-M.Z. acknowledge the finance support from Guangdong Major Project of Basic and Applied Basic Research (2023B0303000026). We thank the staffs from BL19U1 beamline and of National Facility for Protein Science in Shanghai (NFPS) and BL02U1 at Shanghai Synchrotron Radiation Facility, for assistance during data collection.

Author contributions

Z.-M.Z. and J.W. conceived the project, wrote and revised the manuscript. R.Q. contributed to drafting and revising the manuscript. R.Q. and J.C. carried out the cloning and expression of the PTs, protein purification, biochemical kinetics, chemical synthesis and purification of the products. Y. Z. and H. H. performed the computational study. Z.-M.Z. and H.H. crystallized the proteins and determined the structures. L. G. and Q. G. contributed to the analysis of the products. M.L., Y.L. and B.C. contributed to the isolation and structure determination of the products. M.C., H.Y., S.W., Z.Q. and M.J. contributed in the construction of the cascading system. R.Q. and H.H. contributed equally. The article was written on the basis of contributions of all authors. All authors approved the final version of the article.

Competing interests

The authors declare no competing interests.

Additional information

Supplementary information The online version contains supplementary material available at https://doi.org/10.1038/s41467-026-69706-4.

Correspondence and requests for materials should be addressed to Yang Zhou, Zhi-Min Zhang or Jian-bo Wang.

Peer review information *Nature Communications* thanks Wen Shan Yew and the other anonymous reviewers for their contribution to the peer review of this work. [A peer review file is available.]

---

[1] Key Laboratory of Chemical Biology and Traditional Chinese Medicine Research (Ministry of Education) and Key Laboratory of Phytochemistry R&D of Hunan Province, College of Chemistry and Chemical Engineering, Hunan Normal University, Changsha, P. R. China. [2] Department of Microbiology, Zhejiang University School of Medicine, Hangzhou, P. R. China. [3] Key Laboratory of Multiple Organ Failure (Zhejiang University), Ministry of Education, Department of General Intensive Care Unit of the Second Affiliated Hospital (Zhejiang University), Zhejiang University School of Medicine, Hangzhou, P. R. China. [4] Institute of Pharmaceutical Biotechnology Zhejiang University School of Medicine, Hangzhou, P. R. China. [5] State Key Laboratory of Bioactive Molecules and Draggability Assessment, Jinan University, Guangzhou, P. R. China. [6] Key Laboratory of Tea Science of Ministry of Education, College of Horticulture, Hunan Agricultural University, Changsha 410000, P. R. China. [7] State Key Laboratory of Bioreactor Engineering, East China University of Science and Technology, Shanghai 200237, China. [8] College of Life Sciences, Zhejiang University, Hangzhou 310058, P. R. China. [9] These authors contributed equally: Ruiying Qiu, Huisi Huang. ✉ e-mail: zhouyang@jnu.edu.cn; zhangzm@jnu.edu.cn; jwang2023@zju.edu.cn